Physics of Fluids

Fluid–thermal–structure interaction of three heated circular cylinders in tandem at a low Reynolds number of 150

Cite as: Phys. Fluids **34**, 083605 (2022); https://doi.org/10.1063/5.0105014
Submitted: 22 June 2022 • Accepted: 19 July 2022 • Accepted Manuscript Online: 20 July 2022 •
Published Online: 10 August 2022

Hongjun Zhu (朱红钧), Jiawen Zhong (钟家文) and Bin Liu (刘斌)

Physics of Fluids ARTICLE scitation.org/journal/phf

Fluid–thermal–structure interaction of three heated circular cylinders in tandem at a low Reynolds number of 150

Cite as: Phys. Fluids **34**, 083605 (2022); doi: 10.1063/5.0105014
Submitted: 22 June 2022 · Accepted: 19 July 2022 ·
Published Online: 10 August 2022

Hongjun Zhu (朱红钧),[1,a)] Jiawen Zhong (钟家文),[1] and Bin Liu (刘斌)[2]

AFFILIATIONS

[1]State Key Laboratory of Oil and Gas Reservoir Geology and Exploitation, Southwest Petroleum University, 8 Xindu Road, Chengdu, Sichuan 610500, China
[2]Department of Aeronautics, Imperial College London, London SW7 2AZ, United Kingdom

[a)]Author to whom correspondence should be addressed: zhuhj@swpu.edu.cn

ABSTRACT

The fluid–thermal–structure interaction of three identical, heated circular cylinders in tandem with a variable spacing ratio ranging from 4.0 to 10.0 is numerically investigated using the finite element method in this work. The vibration response and vorticity–temperature distribution are examined at the Prandtl number of $Pr = 0.71$ and the Reynolds number of $\mathrm{Re} = 150$ in the reduced velocity range of $1.0 \leq U_r \leq 15.0$. The numerical results indicate that the temperature distribution generally follows the vorticity clusters, presenting a distinct gradient in the wake. Four flow regimes are identified in terms of the interference of shear layers and vortex shedding, that is, continuous reattachment, alternate reattachment, quasi-identical shedding, and co-identical shedding, which are related to the reduced velocity and the spacing ratio. The middle and downstream cylinders experience the wake-induced vibration, and the wake-induced galloping occurs when $U_r > 6$. Compared with an isolated cylinder, the tandem configuration contributes to the drag reduction in the considered range of spacing ratio. Due to the wake interference, the time-averaged Nusselt number Nu^{mean} is lower than that of an isolated cylinder. The heat transfer of the tandem cylinders is closely associated with their hydrodynamic behaviors.

I. INTRODUCTION

The fluid–thermal–structure interaction (FTSI) issue is widely encountered in modern engineering applications, such as nuclear power reactors, chemical processing, heating, and refrigeration. Shell tube arrangement is the common type of heat exchanger, where cool or hot fluid flows over tubes in the array. The fundamental physics of this application is flow around a circular cylinder,[1] and hence, extensive investigations have been conducted in both experimental tests and numerical simulations. The wake instability of a circular cylinder depends on the Reynolds number ($\mathrm{Re} = U_\infty D/\nu$, where U_∞ is the free-stream velocity, D is the cylinder diameter, and ν is the fluid kinematic viscosity). When Re exceeds about 47,[2,3] periodically fluctuating fluid forces are exerted on the cylinder surface due to the existence of alternately shed vortices in the wake. Consequently, the cylinder oscillation is excited, called vortex-induced vibration (VIV). Wake-induced vibration (WIV) or wake-induced galloping (WIG) may occur when multiple cylinders are arranged in tandem or staggered configuration as the result of wake interaction.[4] Particularly, resonance arises when the vortex shedding frequency coincides with the structural natural frequency, resulting in fatigue damage. The flow-induced vibration (FIV), including VIV, WIV, and WIG, is therefore the main factor influencing the service life of heat exchangers.[5] Moreover, the fluid-thermal interaction further complicates the dynamic behavior of multiple cylinders.

In the last few decades, many works have been performed to investigate the FTSI of an isolated cylinder (IC). Schmidt and Wenner[6] first reported the local transport rate from a heated cylinder surface. In 1988, Karniadakis[1] documented the forced convection heat transfer from an isolated cylinder in crossflow at Re up to 200. It was reported that the wake size, the spatial–temporal structure of Karman vortex street, the unsteady lift and drag coefficients, and the unsteady local heat transfer coefficient were in excellent agreement with the available experimental data in the literature.[7,8] Karanth *et al.*[9] examined the vorticity, stream function, and temperature distribution of an isolated cylinder under the condition of forced convection. It was found that the time-averaged Nusselt number (Nu^{mean}) oscillated at

twice the vortex shedding frequency. Cheng *et al.*[10] reported that the heat transfer was enhanced in the vibration lock-on regime, while the influence was tiny outside this lock-on region. Gau *et al.*[11] observed that the heat transfer was enhanced at the front stagnation point of a heated cylinder oscillating in the crossflow direction, while it was suppressed at the two shoulders due to the amplification of flow velocity. Nevertheless, the heat transfer was re-amplified in the decelerated flow region. However, Yang *et al.*[12] reported that the position corresponding to the maximum *Nu* deviated from the front stagnation point for a two-degrees-of-freedom (2DOF) oscillating cylinder. The heat transfer rate was enhanced remarkably as the oscillating frequency approached the vortex shedding frequency, with the presence of 2S (two vortices were shed per cycle with one shed from the upper side and the other shed from the lower side) shedding and "figure-eight" vibration trajectories.[12–15] When Re exceeds 400,[14] the enhancement of heat transfer became more distinct. It was reported that the heat transfer rate of an oscillating circular cylinder was increased by 13% in comparison with the stationary one.[13] Furthermore, the dynamic and thermal behaviors of the cylinder were affected by the in-line oscillation,[15] presenting the best heat transfer performance at $U_r = 6$ in the two-degrees-of-freedom (2DOF) FIV case[12] and $U_r = 4$ in the transverse vibration case only.[16]

When one cylinder is placed in the wake of another, the occurrence of hydrodynamic interference will result in different structural dynamic responses and heat transfer performance as compared with the isolated cylinder (IC). Igarashi[17,18] and Zdravkovich[19–21] carried out experimental studies on the FIV of two tandem circular cylinders. In 1987, Zdravkovich[20] reviewed the relevant literature and classified the flow structures into three regimes: (1) overshoot flow regime occurring at $1 < L/D < 1.2$–1.8 (where L is the center-to-center distance between two tandem cylinders), where the upstream-cylinder-generated shear layers overpassed the downstream cylinder and alternately shed vortices prevailed behind the downstream cylinder; (2) reattachment flow regime taking place at $1.2–1.8 < L/D < 3.4–3.8$, where the upstream-cylinder-generated shear layers reattached on the downstream cylinder surface and quasi-steady recirculation was formed in the gap between the cylinders; (3) co-shedding flow regime ($L/D > 3.4–3.8$), where the vortices were also shed from the upstream cylinder surface and then were convected in the gap. Alam *et al.*[22] further divided the reattachment flow regime into alternate and steady reattachment sub-patterns with the critical spacing ratio around $L/D \sim 3.0$, while Zhu and Wang[23] named the latter as the continuous reattachment pattern. Zhu *et al.*[24] proposed a new flow pattern based on the numerical results of flow around three isodiametric circular cylinders with identical spacing. This flow pattern occurring at $3.5 < L/D < 6.5$ was named a quasi-co-shedding (QCS) regime, where the downstream cylinder was sandwiched between two shear layers detached from the middle one, and two same-sign vortices in each shear layer coalesced into a larger vortex in the far wake. Therefore, the vibration response of three tandem cylinders significantly depends on L/D. Chen *et al.*[25] numerically observed two different vibration patterns: wake-induced galloping (WIG) when $L/D = 1.2$ and vortex-induced vibration (VIV) when $L/D = 1.5$–5.0. The major difference is that the former presents the divergent vibrations with the increasing reduced velocity. The two-degrees-of-freedom (2DOF) vibration of three tandem cylinders is investigated by Gao *et al.*[26] and Tu *et al.*[27] Gao *et al.*[26] proposed six flow regimes, that is, single bluff body flow, alternating shear layer reattachment flow, deflected gap flow, two parallel vortex streets with co-shedding flow, chaotic wake, and 2S wake flow. Tu *et al.*[27] classified the vibration orbits into six patterns, including eight-figure, raindrop, oval, dual-raindrop, dual-eight, and dual-oval sharp shapes.

Taking into account the heat transfer in the two-tandem-cylinder case, Mahir and Altaç[28] found that the Nu^{mean} of the upstream cylinder approached that of an isolated isothermal cylinder, while the Nu^{mean} of the downstream cylinder was about 80% of the upstream cylinder at $L/D > 4$. Patil *et al.*[29] numerically observed that the larger the spacing ratio, the closer the behavior of the downstream cylinder to an isolated one, suggesting the weakened wake interference between the cylinders. Sun *et al.*[30] reported that the interference between the downstream cylinder and the wake of the upstream cylinder has a little effect on the upstream cylinder, while it influences the wake pattern, fluid forces, and response and heat transfer of the downstream one in the co-shedding regime. Numerical investigations of flow and heat transfer characteristics of two tandem circular cylinders in different diameters at low Reynolds numbers were conducted by Mahir and Altaç[31] and Zafar and Alam.[32] The heat transfer phenomenon was observed to be sensitive to spacing ratio and Re. Zafar and Alam[32] identified a tertiary frequency from the fluctuation of heat transfer, through both the fast Fourier transform and wavelet analysis. Harimi and Saghafian[33] also reported that the force coefficients and the wake structure depended on the spacing ratio.

Nevertheless, the aforementioned studies were mainly performed within a narrow spacing ratio range, and little literature took into account the convection heat transfer process. In the present paper, therefore, the FTSI of three tandem cylinders in a wider spacing ratio is numerically investigated to further understand the interaction between 2DOF FIV response and convection heat transfer behavior. As the spacing ratio in a limited range of $L/D = 1.05$–5.5 has been investigated in previous literature,[25,27,34] the spacing ratio in a broader range of $L/D = 4$–10 is considered in this work. The Prandtl number ($Pr = \mu/\rho\alpha$, where ρ is the fluid density, μ is the dynamic viscosity of fluid, and α is the thermal diffusivity) is fixed at $Pr = 0.71$, which is widely adopted in previous FTSI kinds of literature.[10] The simulation of the FTSI of three tandem cylinders is conducted in the reduced velocity range of 1–15, which is a typical range in both natural and engineering applications.[25–27]

II. GOVERNING EQUATIONS AND NUMERICAL METHODS

A. Governing equations and problem description

The unsteady Navier–Stokes equations are coupled with the conservation of energy equation in this work to simulate the heat transfer and flow around three tandem cylinders. The governing equations and associated boundary and initial conditions are expressed as follows:

$$\nabla \cdot \boldsymbol{u} = 0, \qquad \forall \boldsymbol{x} \in \Omega^f(t), \tag{1a}$$

$$\rho(\partial_t \boldsymbol{u} + (\boldsymbol{u} \cdot \nabla)\boldsymbol{u}) = \nabla \cdot \boldsymbol{\sigma}, \quad \forall \boldsymbol{x} \in \Omega^f(t), \tag{1b}$$

$$\partial_t T + (\boldsymbol{u} \cdot \nabla)T = \alpha \nabla^2 T, \quad \forall \boldsymbol{x} \in \Omega^f(t), \tag{1c}$$

$$\boldsymbol{u} = \tilde{\boldsymbol{u}}; \quad \boldsymbol{T} = \tilde{\boldsymbol{T}}, \quad \forall \boldsymbol{x} \in \Gamma_D^f(\boldsymbol{t}), \tag{1d}$$

$$\boldsymbol{\sigma} \cdot \boldsymbol{n} = \tilde{\boldsymbol{h}}; \quad \boldsymbol{\alpha}(\nabla \boldsymbol{T}) \cdot \boldsymbol{n} = \tilde{\boldsymbol{q}}, \quad \forall \boldsymbol{x} \in \Gamma_N^f(\boldsymbol{t}), \tag{1e}$$

$$\boldsymbol{u} = \tilde{\boldsymbol{u}}_0; \quad T = \tilde{T}_0, \quad \forall \boldsymbol{x} \in \Omega^f(0), \tag{1f}$$

where $\boldsymbol{u}$ is the flow velocity vector, $\boldsymbol{x}$ is the position vector, ρ is the fluid density, p is the pressure, t is the flow time, $\boldsymbol{\sigma}$ is the Cauchy stress tensor, T is the temperature, α is the thermal diffusivity, $\tilde{\boldsymbol{u}}$ represents the prescribed flow velocity imposed along the boundaries, $\tilde{T}$ represents the prescribed temperature imposed along the boundaries, $\boldsymbol{n}$ is the unit outward normal vector of the element's edge, $\tilde{\boldsymbol{h}}$ and $\tilde{q}$ are the prescribed convection transfer coefficient and heat flux along the boundaries, respectively, $\tilde{\boldsymbol{u}}_0$ represents the initial flow velocity, $\tilde{T}_0$ represents the initial temperature, and Γ_D and Γ_N denote the Dirichlet and Neumann domain boundaries, respectively. The term $\partial_t(\cdot)$ represents the partial derivative with respect to the flow time. The Cauchy stress tensor ($\boldsymbol{\sigma}$) is a function of $\boldsymbol{u}$ and p, defined as

$$\boldsymbol{\sigma} = -p\boldsymbol{I} + 2\mu\boldsymbol{\varepsilon}, \tag{2a}$$

$$\boldsymbol{\varepsilon} = \frac{1}{2}\left[\nabla\boldsymbol{u} + (\nabla\boldsymbol{u})'\right], \tag{2b}$$

where $\boldsymbol{I}$ is the Kronecker matrix, μ is the dynamic viscosity, $\boldsymbol{\varepsilon}$ is the strain rate tensor, and the superscript ($'$) is a transpose operator.

The dynamic response of each elastically mounted cylinder is modeled by a mass–spring system as follows:

$$\ddot{\boldsymbol{x}} + \frac{4\pi\zeta}{U_r}\dot{\boldsymbol{x}} + \frac{4\pi^2}{U_r^2}\boldsymbol{x} = \frac{\boldsymbol{F}}{2m^*}, \tag{3}$$

where $\ddot{\boldsymbol{x}}$, $\dot{\boldsymbol{x}}$, and $\boldsymbol{x}$ denote the acceleration vector, velocity vector, and displacement vector of the cylinder, respectively; ζ is the structural damping ratio, defined as 0 in present work; and m^* is the reduced mass, defined as 2.0 ($m^* = m/\rho D^2$), where m is the mass of the cylinder per unit length. The non-dimensional force component is $C_D = 2F_D/\rho U_{in}^2 D$ and $C_L = 2F_L/\rho U_{in}^2 D$, where $\boldsymbol{F}(F_D, F_L)$ is the fluid force acting on the cylinder surface in the streamwise and transverse directions, and U_{in} is the free stream velocity. The reduced velocity U_r is defined as $U_r = U_{in}/f_n D$, where f_n is the natural frequency of the structure in stagnant fluid $f_n = (1/2\pi)\sqrt{k/m}$ and k is the stiffness of spring.

An arbitrary Lagrangian–Eulerian (ALE) description is employed to track the fluid–structure interface. The Navier–Stokes equation and the conservation of energy equation are spatially discretized using the stabilized finite element formulation in ALE description. For the detailed formulation, we refer to Liu and Zhu.[35] The unconditionally stable second-order accurately generalized–α time integration scheme is employed for both fluid and structure solvers to march the solutions in time, which has been proved to be feasible by Chung and Hulbert[36] and Jansen *et al.*[37]

The temperature is normalized by the maximum temperature differences expressed as $T^* = (T - T_{min})/(T_{max} - T_{min})$, where the T^* is the normalized temperature, and T_{max} and T_{min} represent the maximum and minimum temperatures in the computational domain, respectively. In the simulation, the normalized temperature of the surfaces of three tandem cylinders is identically defined as 1 ($T^* = 1$). The local Nusselt number $Nu(s)$ of a specific location on the cylinder surface and the Nu of the entire cylinder surface are defined as

$$Nu(s) = -\nabla T^*(s) \cdot \boldsymbol{n}(s), \tag{4a}$$

$$Nu = \frac{1}{\ell}\int_{s=0}^{\ell} Nu(s)ds. \tag{4b}$$

Figure 1 illustrates the employed computational domain and associated boundaries. The upstream cylinder is initially placed at the origin ($x = 0$, $y = 0$), and the computational domain extends $50D$ downstream and $10D$ upstream from this cylinder center. The streamwise spacing between the upstream cylinder (denoted as C1) and the middle cylinder (denoted as C2) is identical to that between the middle cylinder and the downstream one (denoted as C3), ranging from $4D$ to $10D$ with an increment of $2D$. The tandem cylinders are placed centrally in the transverse direction. Consequently, the blocking ratio is about 1.67%, meeting the requirement of a blocking ratio less than 6%.[38,39]

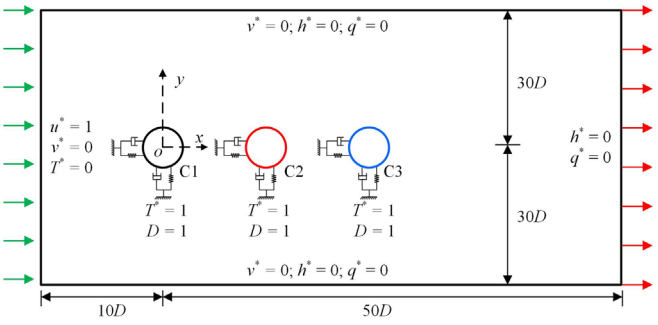

FIG. 1. Computational domain and boundary conditions.

The boundary conditions are also highlighted in Fig. 1. A Dirichlet-type boundary condition is adopted at the inlet with $u^* = 1$, $v^* = 0$, and $T^* = 0$, where the superscript ($*$) denotes the associated dimensionless parameters. A Neumann-type (traction-free) boundary condition is applied at the outlet with $h^* = 0$ and $q^* = 0$. The two lateral boundaries are defined as the symmetry boundary condition with $v^* = 0$, $h^* = 0$, and $q^* = 0$.The no-slip boundary condition is prescribed over the cylinders' surface in accompany with the uniform temperature ($T^* = 1$). To account for the cylinder's motion, its velocity components in the x and y directions are updated on the surface for every nonlinear iteration. The hydrodynamic and thermal characteristics of the vibrating cylinders are examined in a spacing ratio of $L/D = 4$–10 with the reduced velocity ranging from 1 to 15. The Reynolds number and the Prandtl number are fixed at $Re = 150$ and $Pr = 0.71$, respectively.

B. Spatial and temporal convergence analysis

In this investigation, the computational domain, $60D \times 60D$, is structurally meshed by Gmsh in Fig. 2(a), where D is the diameter of the cylinder. A non-uniform grid distribution was employed with a more refined grid generated around three circular cylinders wall, and the smallest normalized grid height near the cylinder surface is set to 0.025 with $y^+ = 0.375$ less than 1. The grid was further refined along a rectangular region encompassing the cylinder(s) to accurately capture the wake and vortex street behind the cylinder(s). A close-up view of the mesh around a cylinder is shown in Fig. 2(b). The mesh is made up of a structured part near the cylinder's surface, which is adequately refined to capture the boundary layer. The unstructured part of the mesh is created via Delaunay's triangulation technique.

The mesh convergence analysis is carried out for the simulation of flow over the three circular cylinders with $L/D = 4$ in forced convection flow at $U_r = 6$. From Table I, it is evident that the error of the hydrodynamic and thermal response is within 1% for the mesh

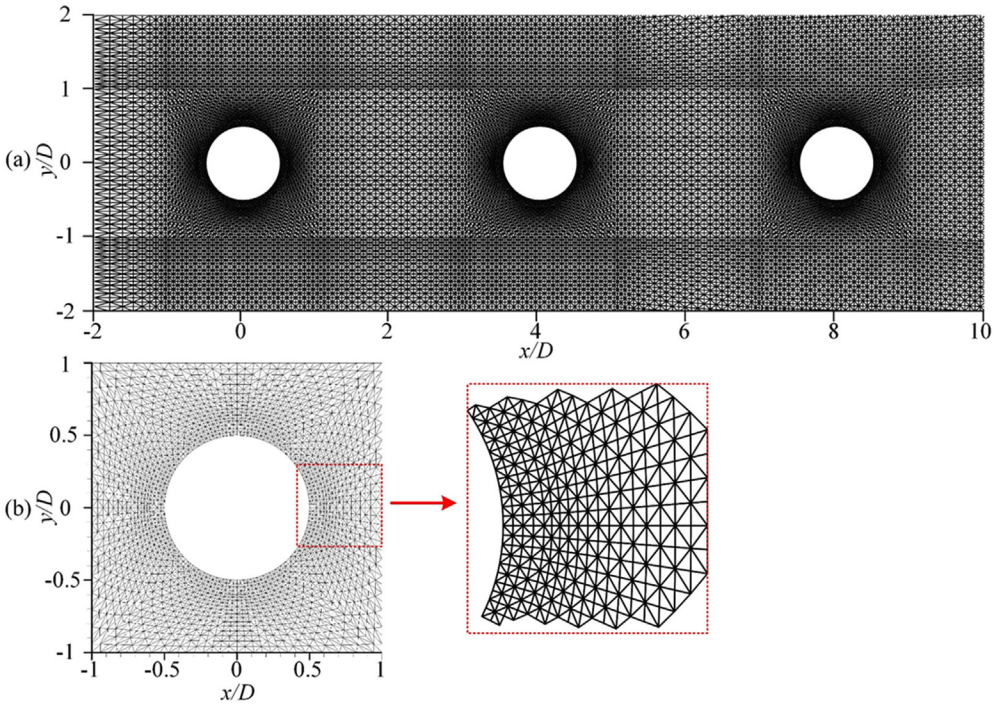

FIG. 2. Finite-element mesh structure: (a) grid distribution around three circular cylinders in tandem and (b) grids in the vicinity of one cylinder and the boundary-layer elements.

resolution M2, where C_D^{mean}, C_L^{RMS}, St, and Nu^{mean}, respectively, are the mean drag coefficient, the root means square lift coefficient, the Strouhal number, and the mean Nusselt number. Hence, M2 is used for all simulations in this article. Note that the simulation of each case is carried out until enough periodic results are obtained after a statistically stable flow state has been reached.

The results of the time convergence analysis together with the approximated maximum Courant–Friedrichs–Lewy (CFL) numbers are listed in Table II. Since the unconditionally stable second-order accurate generalized α implicit time integration is used for fluid formation,[35] the restriction of critical CFL number is less than the other explicit time integration schemes to satisfy the stability requirement. In terms of accuracy, the time convergence analysis in Table II shows that the time step $dt = 0.01$ is optimal for the investigation of forced convection flow, where the errors of the hydrodynamic and thermal response are within ±1% compared with the referential values at $dt = 0.005$. Hence, the time step $dt = 0.01$ is used for all simulations in this article.

C. Code validation

The derived numerical formulation is validated for the flow around a heated isolated circular cylinder at $Pr = 1$ and 10 and flow past an elastically mounted circular cylinder at $\mathrm{Re} = 150$, $m^* = 2.0$, $\zeta = 0$, and $U_r = 1$–10, as illustrated in Fig. 3, respectively. Detailed code validation is done for an isolated cylinder in Liu and Zhu.[35] It can be seen that the obtained mean Nusselt numbers from the derived formulation for heat convection flow match well with the literature[40–42] and the empirical formula[42] in Eq. (5), as shown in Fig. 3(a)

$$Nu^{mean} = 0.3 + \frac{0.62\mathrm{Re}^{1/2}\mathrm{Pr}^{1/3}}{\left[1 + (0.4/\mathrm{Pr})^{2/3}\right]^{1/4}}\left[1 + \left(\frac{\mathrm{Re}}{282\,000}\right)^{5/8}\right]^{4/5}. \quad (5)$$

The structural dynamics obtained from the implemented ALE formulation are validated by comparing the values of the dimensionless transverse fluctuation in literature.[43–46] The root-mean-squared (RMS) transverse fluctuation is expressed as

$$A_y^{RMS} = \sqrt{\frac{\sum_i^N \left(A_y(i) - A_y^{mean}\right)^2}{N}}, \quad (6)$$

where A_y^{RMS} and A_y^{mean} are the root-mean-squared (RMS) transverse fluctuation and the mean transverse displacement of the cylinder, respectively. The value of N is the total number of sampled data. Figure 3(b) shows the good agreement of the VIV lock-in response with the literature.

III. RESULTS AND DISCUSSION

A. Wake structure and evaluation

Based on the identification method proposed by Zdravkovich[19–21] and Zhu *et al.*,[23,24] four flow regimes are observed between two adjacent cylinders, including the continuous reattachment (CR),[23] the alternate reattachment (AR), the quasi-co-shedding (QCS),[24] and the co-shedding (CS) regimes, respectively. Figure 4 illustrates the six wake interference regimes observed in this study as the values of L/D and U_r increase, for example, CR–AR, AR–AR,

TABLE I. Results of different mesh resolutions for flow past three circular cylinders with $L/D = 4$ in forced convective flow at $U_r = 6$.

		C1				C2				C3			
Mesh	Elements	C_D^{mean}	C_L^{RMS}	St	Nu^{mean}	C_D^{mean}	C_L^{RMS}	St	Nu^{mean}	C_D^{mean}	C_L^{RMS}	St	Nu^{mean}
Mesh1	63 737	1.688 (0.00%)	0.163 (0.61%)	0.160 (0.00%)	6.522 (0.02%)	0.768 (0.13%)	0.506 (4.35%)	0.127 (0.79%)	5.044 (0.75%)	0.091 (1.10%)	0.437 (1.60%)	0.127 (0.79%)	2.844 (0.21%)
Mesh2	81 777	1.688 (0.00%)	0.164 (0.00%)	0.160 (0.00%)	6.523 (0.00%)	0.769 (0.26%)	0.528 (0.38%)	0.128 (0.00%)	5.082 (0.04%)	0.092 (0.00%)	0.444 (0.23%)	0.128 (0.00%)	2.850 (0.04%)
Mesh3	100 787	1.688	0.164	0.160	6.523	0.771	0.530	0.128	5.084	0.092	0.445	0.128	2.851

TABLE II. Results of different time steps for flow past three circular cylinders with $L/D = 4$ in forced convective flow at $U_r = 6$, using Mesh2 (85762).

	C1				C2				C3				
Time steps	C_D^{mean}	C_L^{RMS}	St	Nu^{mean}	C_D^{mean}	C_L^{RMS}	St	Nu^{mean}	C_D^{mean}	C_L^{RMS}	St	Nu^{mean}	Max CFL
$dt = 0.020$	1.686 (−0.24%)	0.179 (9.82%)	0.159 (−0.63%)	6.522 (0.02%)	0.703 (−9.39%)	0.482 (−9.57%)	0.123 (−3.9%)	4.890 (−4.36%)	0.085 (−7.61%)	0.425 (−4.92%)	0.123 (−4.65%)	2.620 (−8.74%)	1.686
$dt = 0.010$	1.688 (−0.12%)	0.164 (0.61%)	0.160 (0.00%)	6.523 (0.03%)	0.769 (−0.91%)	0.528 (−0.94%)	0.128 (0.00%)	5.082 (−0.61%)	0.092 (0.00%)	0.444 (−0.67%)	0.128 (−0.78%)	2.850 (−0.73%)	0.873
$dt = 0.005$	1.690	0.163	0.160	6.521	0.776	0.533	0.128	5.113	0.092	0.447	0.129	2.871	0.410

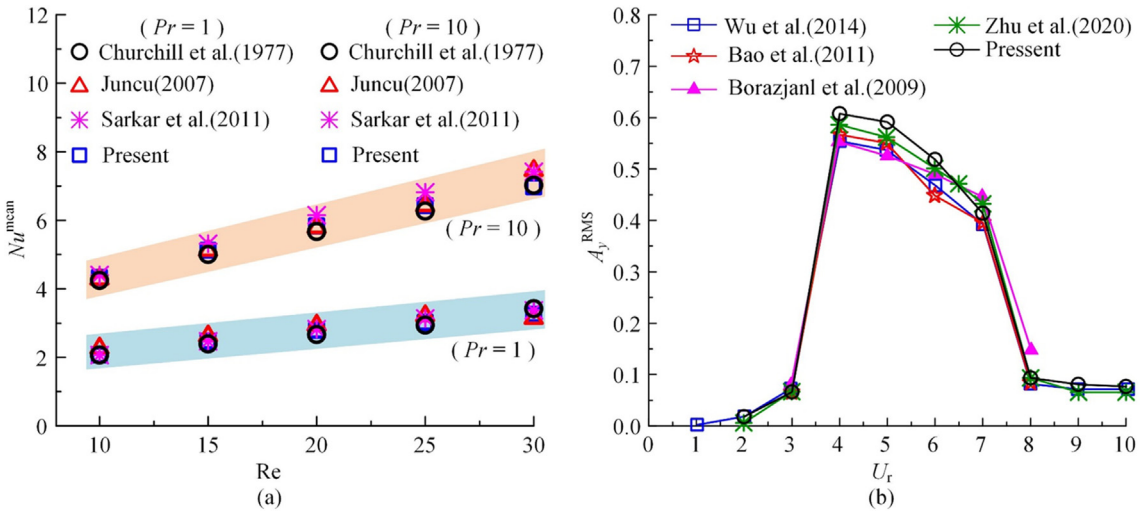

FIG. 3. Validation of the implemented numerical algorithm: (a) flow past a circular cylinder in forced convection flow at $Pr = 1$ and $Pr = 10$; (b) flow past an elastically mounted cylinder ($m^* = 2.0$ and $\zeta = 0$) in $U_r = 1$–10 at Re = 150.

AR–QCS, AR–CS, CS–QCS, and CS–CS. In the subsequent discussion, the upstream, middle, and downstream cylinders are referred to as C1, C2, and C3, respectively. When the initial center-to-center spacing ratio is $L/D = 4.0$ and the reduced velocity is $U_r < 3$, it is found that the wake interference regime between the adjacent cylinders is the AR–QCS regime, whereas, as the reduced velocity increases ($3 \leq U_r < 5$), the AR–QCS wake interference regime changes to the CR–AR regime. On the other hand, when the reduced velocity increases further ($5 \leq U_r < 8$), the wake interference regime switches back to the AR–QCS regime again. When the reduced velocity exceeds $U_r \geq 8$, the wake interference regime between the cylinder C2 and the cylinder C3 changes to the AR regime instead. If the initial center-to-center spacing ratio is at $L/D = 6.0$, the wake interference regime between the cylinder C1 and the cylinder C2 changes from the CS regime to the AR regime at $U_r = 8$. Meanwhile, it is also noticed that the wake interference regime between the cylinder C2 and the cylinder C3 varies from the QCS regime to the CS regime at $U_r = 4$. Additionally, as the spacing ratio continues increasing, the CS regime is only observed between the cylinder C1 and the cylinder C2 and the QCS regime only appears between the cylinder C2 and the cylinder C3 at $L/D = 8.0$ and $U_r = 3$.

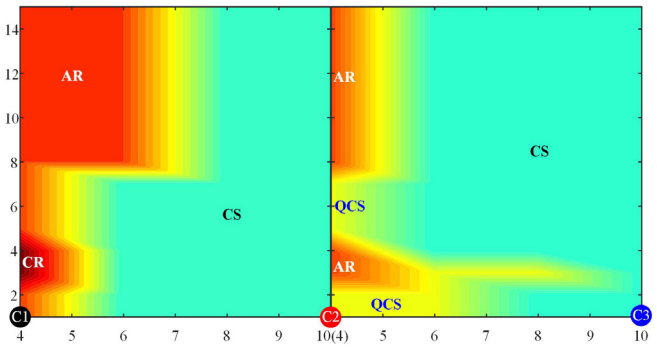

FIG. 4. The classification of wake interference pattern for the three vibrating cylinders in tandem arrangements, where CR denotes the continuous reattachment regime, AR denotes the alternate reattachment regime, and CS and QCS represent the co-shedding and quasi-co-shedding regimes, respectively.

The complex coupling between fluid hydrodynamics, thermal energy transport, and structural dynamics among three vibrating tandem cylinders in forced convection is phenomenal. As illustrated in Figs. 4 and 5, when the initial spacing ratio is $L/D = 4.0$, both of them present the characteristics similar to those of circumferential flow at low reduced velocity values ($U_r < 3$). Figure 5 shows that the shed vortex of the upstream cylinder alternatively attaches to the surface of the middle cylinder and contributes to the vortex shedding of the middle cylinder. Further downstream, the shed vortices from the middle cylinder form a double row vortex in wake and inhibit the vortex shedding behind the downstream cylinder. In this case, there is no vortex shedding behind the downstream cylinder, and it is in the quasi-stable process to transit from the reattachment regime to the co-shedding regime. Therefore, the wake interference regime in this case is called the AR–QCS regime. However, as the reduced velocity keep increasing, the vibration amplitudes of the three tandem cylinders show a rising tendency, especially for the streamwise vibration. For $3 \leq U_r < 5$, it is found that the vortex shedding of the upstream cylinder is inhibited, and its shear layers directly re-attach to the middle cylinder, as shown in Fig. 5. The shed vortices from the middle cylinder re-attach to the downstream cylinder again and subsequently coalesces with the shed large vortices behind the downstream cylinder. For this reason, this wake interference mode observed between the upstream-to-middle cylinders and the middle-to-downstream cylinders is defined as the CR–AR regime. As the value of reduced velocity keeps increasing, the cylinder C1 and the cylinder C2 always manifest the alternating reattachment (AR) regime, whereas the cylinder C2 and the cylinder C3 undergo the QCS regime for the range $5 \leq U_r < 8$. Due to the small initial center-to-center spacing, the shear layers behind the middle cylinder alternatively re-attach to the downstream cylinder before separating and forming the vortices downstream. This shows the typical

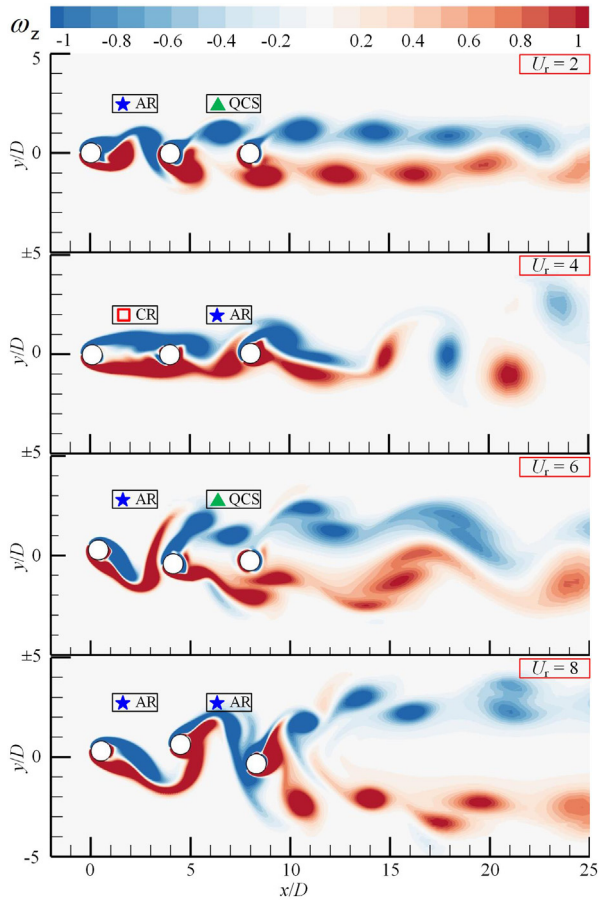

FIG. 5. Flow structure at $L/D = 4.0$ and $tU_\infty/D = 300$ for $U_r = 2$, 4, 6, and 8, respectively.

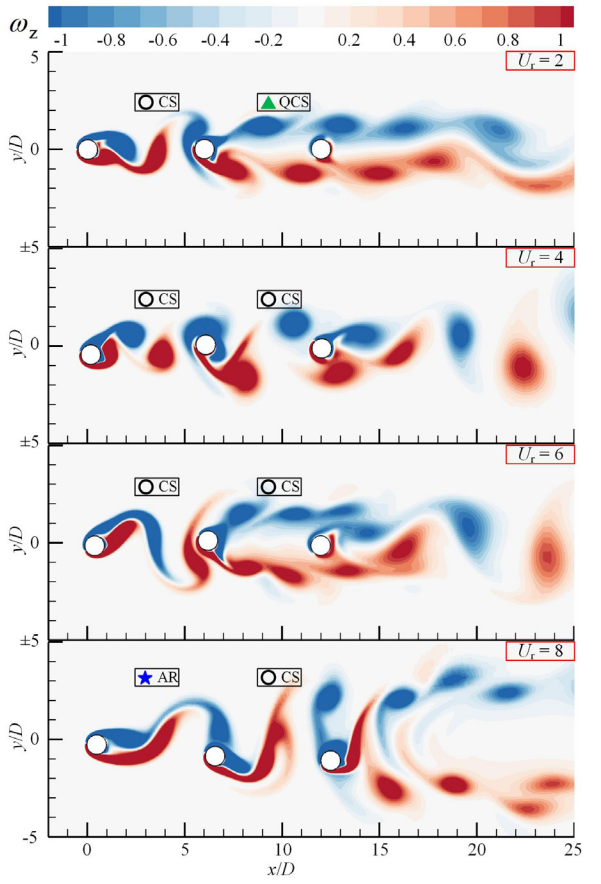

FIG. 6. Flow structure at $L/D = 6.0$ and $tU_\infty/D = 300$ for $U_r = 2$, 4, 6, and 8, respectively.

characteristics of the AR regime. As depicted in Fig. 5, the vortex shedding behind the middle cylinder is wider for $5 \leq U_r < 8$, owing to the increased vibrating amplitudes of both the cylinder C1 and the cylinder C2. Since the downstream cylinder is in the shadowing flow, the vortex shedding around the downstream cylinder is suppressed. Consequently, this quasi-stable process of the transition from the reattachment regime to the co-shedding regime is classified as the QCS regime.

As exhibited in Figs. 4 and 6, when the initial center-to-center spacing is $L/D = 6.0$ and the reduced velocity is $U_r < 8$, the boundary layer separated from the upstream cylinder has a sufficient distance to curl and form the vortices. The shed vortices from the upstream cylinder impinge the middle cylinder in the backward migration process and fuse with the vortices behind the middle cylinder. Figure 6 shows that the shed vortices behind both the cylinder C1 and the cylinder C2 manifest the characteristics of the CS wake interference regime. For $8 \leq U_r \leq 15$, because the shear layers separated from the upstream cylinder are significantly stretched, they alternatively re-attach to the middle cylinder before shedding further downstream. As exhibited in Fig. 5, the shear layers shed behind the middle cylinder form strong vortex clusters. It implies that a large amount of fluid kinetic energy is transported from the shear layers of the upstream cylinder. This is one of the typical characteristics of the AR regime. When the reduced velocity is $U_r < 4$, the hydrodynamics around the cylinder C2 and the cylinder C3 is similar to the steady flow around the three circular cylinders in tandem,[24] in which there is no vortex shedding behind the downstream cylinder. This is the quasi-stable process of the transition from the reattachment to the homogeneity shedding regime, which is classified as the QCS regime. With the increase in reduced velocity ($4 \leq U_r \leq 15$), the shed vortices behind the middle cylinder re-attach to the downstream cylinder again in the process of the backward migration. Meanwhile, the downstream cylinder also formed large shed vortex clusters further downstream. This regime is termed as the co-shedding CS regime. Nevertheless, as the reduced velocity keeps increasing, there are three different forms of co-shedding regime. (1) The shed vortices behind the middle cylinder impinge the boundary layer of the downstream cylinder for $U_r = 4$, which transfers a large amount of fluid kinetic energy into the wake of the downstream cylinder and results in the 2S model of wake pattern. (2) The shed vortices behind the middle cylinder coalesce with the vortices behind the downstream cylinder and manifest the 2S mode of wake pattern for $U_r = 6$. (3) The shed vortices from the middle cylinder do not coalesce with the vortices behind the downstream cylinder in this case and

exhibit a double-row vortex migrating with the backward wake for $U_r = 8$ instead. Consequently, the vortex shedding overtly occurs behind both the cylinder C2 and the cylinder C3 in the double-row vortex pattern.

As illustrated in Figs. 4 and 7, when the initial center-to-center spacing is $L/D = 8.0$, the vortex shedding behind the cylinder C1 and the cylinder C2 have enough space to develop and form strong vorticity clusters. Hence, the wake interference regimes are always the CS regime in this case. It is also observed that a double row of vortex shedding appears behind the middle cylinder for $U_r < 4$. As the reduced velocity increases, the location of the merged double row of vortex shedding, at where the secondary vortex forms, gradually moves forward. Meanwhile, it is also found that the vortex shedding merging process merely happens around the downstream cylinder for $U_r \leq 2$, as shown in Fig. 7. Accordingly, the shed vortices behind the middle cylinder reattach to the downstream cylinder, transfer strong fluid kinetic energy into the shear layer of the downstream cylinder, and trigger the vortex shedding of the downstream cylinder subsequently. Therefore, it is found that the vortex shedding process happens on both the cylinder C2 and the cylinder C3 in the CS regime. By contrast, when the reduced velocity is $U_r = 3$, the position of the secondary vortices formed by the coalescence of the double-row vortices is

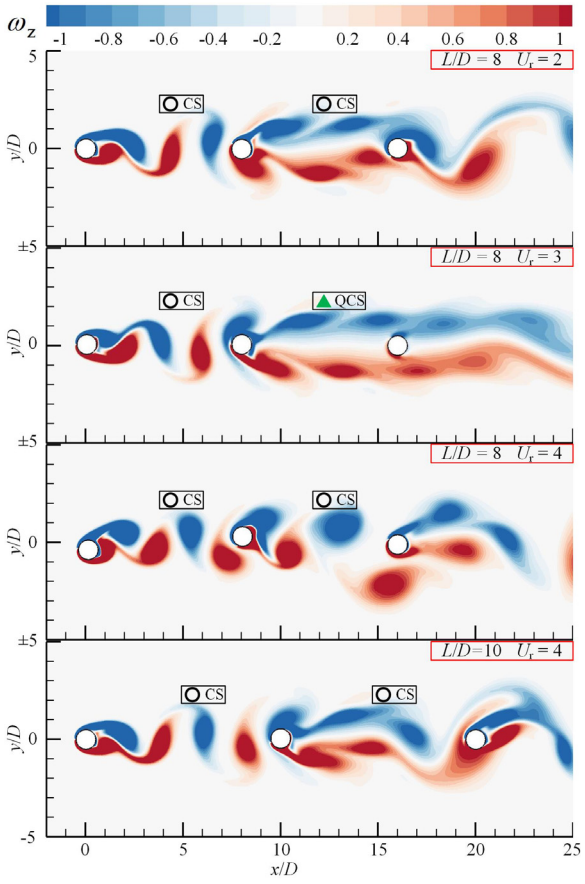

FIG. 7. Flow structure at $L/D = 8.0$ and $tU_\infty/D = 300$ for $U_r = 2$, 3, 4, and $L/D = 10.0$ at $tU_\infty/D = 300$ for $U_r = 4$, respectively.

behind the downstream cylinder, as shown in Fig. 7. As a result, the vortex formation behind the downstream cylinder is inhibited and the downstream cylinder is in the quasi-stable process of transition from the reattachment to the co-shedding regime, which manifests the characteristics of the QCS regime. As the reduced velocity increases further, as illustrated in Fig. 7, the vortex shedding behind the middle cylinder no longer sustains a double-row structure for $U_r \geq 4$, but exhibits a 2S mode of wake pattern. Furthermore, it is found that the vortex shedding also happens behind the downstream cylinder. Consequently, the observed wake interference between the cylinder C2 and the cylinder C3 for $4 \leq U_r \leq 15$ is classified as the CS regime. Additionally, when the center-to-center spacing is $L/D = 10$, as depicted in Figs. 4 and 7, the vortex shedding occurs on all three tandem cylinders at the same time in a row. In fact, they are all associated with the same CS regime, collectively.

B. Flow-induced vibration in forced convection

In this session, the structural dynamics of three vibrating tandem cylinders is investigated. As the instantaneous center-to-center distances between cylinders change during the structural vibration, the wake dynamics and thermal energy transport behind each cylinder are significantly affected. Simultaneously, the complicated coupling between hydrodynamics and heat convection in forced convection also induces a strong nonlinearity in the structural dynamics and results in complex structural dynamics, vice versa. Especially, in regard to the heat convection process, the thermal convection efficiency (Nu) around the vibrating cylinders is drastically modulated because of the mutual interference between the wake and structural dynamics between the tandem cylinders. Eventually, the fluid-induced vibration of three tandem cylinders exhibits itself as a highly nonlinear fluid–thermal–structure coupling problem in engineering design involving thermofluids.

When studying the interaction between the vibrating tandem cylinders, the center-to-center spacing is usually taken as a dependent variable parameter to carry out the investigation. The mutual interference between the tandem cylinders has always been one of the critical issues in research of wake interference. In this study, the VIV response of an isolated cylinder (IC) with the same dimensionless groups ($\mathrm{Re} = 150$, $m^* = 2.0$, $1.0 \leq U_r \leq 15.0$, and $\zeta = 0$) is taken as the reference for comparison. It can be seen in Fig. 8(a) that the mean streamwise displacement of the upstream cylinder, Xmean 1, is consistent with that of the isolated cylinder and increases exponentially for $U_r = 1$–4. On the other hand, it is observed that the mean streamwise displacement X^{mean} of both the isolated cylinder and the upstream cylinder increase linearly for $U_r = 8$–15. The mean streamwise displacement X^{mean} of an isolated cylinder is about $1.83\,U_r = 15$; whereas the mean streamwise displacement Xmean 1 of the upstream cylinder falls between 1.61 and 1.73. In terms of the cylinder C2, it is found that its mean streamwise displacement Xmean 2 is lower than that of the isolated cylinder for $U_r = 1$–5. As the reduced velocity increases further $U_r = 6$–8, the mean streamwise displacement of the middle cylinder becomes higher than that of the isolated cylinder instead, but obviously its value decreases subsequently as the reduced velocity keep increasing. It is also noticed that the mean streamwise displacement of the middle cylinder Xmean 2 gradually increases along a straight line for $U_r = 9$–15, but it is still lower than that of the isolated cylinder. Also, because of the existence of the cylinder C1 and the cylinder C2, it is realized that the mean streamwise displacement of the

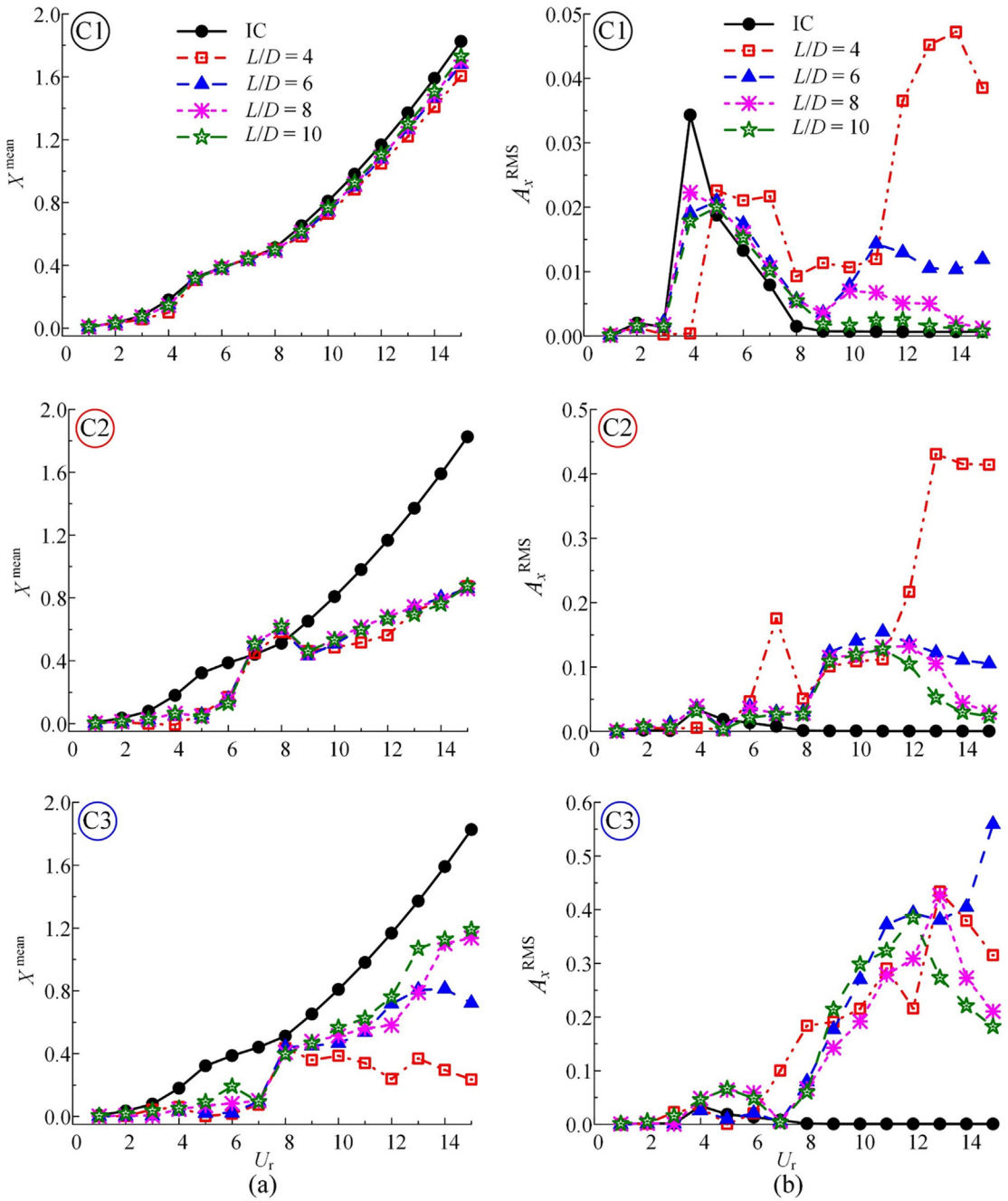

FIG. 8. (a) Time-averaged displacement (X^{mean}) and (b) associated RMS amplitude in the streamwise direction (A_x^{RMS}).

downstream cylinder *X*mean 3 has an abrupt change within the range of $U_r = 6$–8. By contrast, the mean streamwise displacement of the downstream cylinder *X*mean 3 is found always lower than that of the isolated cylinder.

In regard to the root-mean-squared (RMS) value of the streamwise vibration of an isolated cylinder and three tandem cylinders A_x^{RMS}, Fig. 8(b) shows that the RMS values of the streamwise vibration are both $A_{x1}^{RMS} \leq 0.05$ for an isolated cylinder and the upstream cylinder. On the other hand, the RMS values of the streamwise vibration become $A_{x2}^{RMS} \leq 0.5$ for the middle cylinder and $A_{x3}^{RMS} \leq 0.6$ for the downstream cylinder, respectively, in tandem arrangement. In this study, A_x^{RMS} is defined as the vibration

amplitude offset against the mean streamwise displacement of that cylinder X^{mean} during vibration. In order to statistically determine the deviation scope of one cylinder from its initial position, the associated maximum and minimum values of the streamwise displacement can be expressed as[35]

$$X^{\max} = X^{\mathrm{mean}} + \sqrt{2}A_x^{\mathrm{RMS}}, \quad X^{\min} = X^{\mathrm{mean}} - \sqrt{2}A_x^{\mathrm{RMS}}, \tag{7}$$

where $X^{\max}$ and $X^{\min}$ are the statistical maximum and minimum streamwise displacements based on the initial position, respectively, and X^{mean} is the mean streamwise displacement, as shown in Fig. 9.

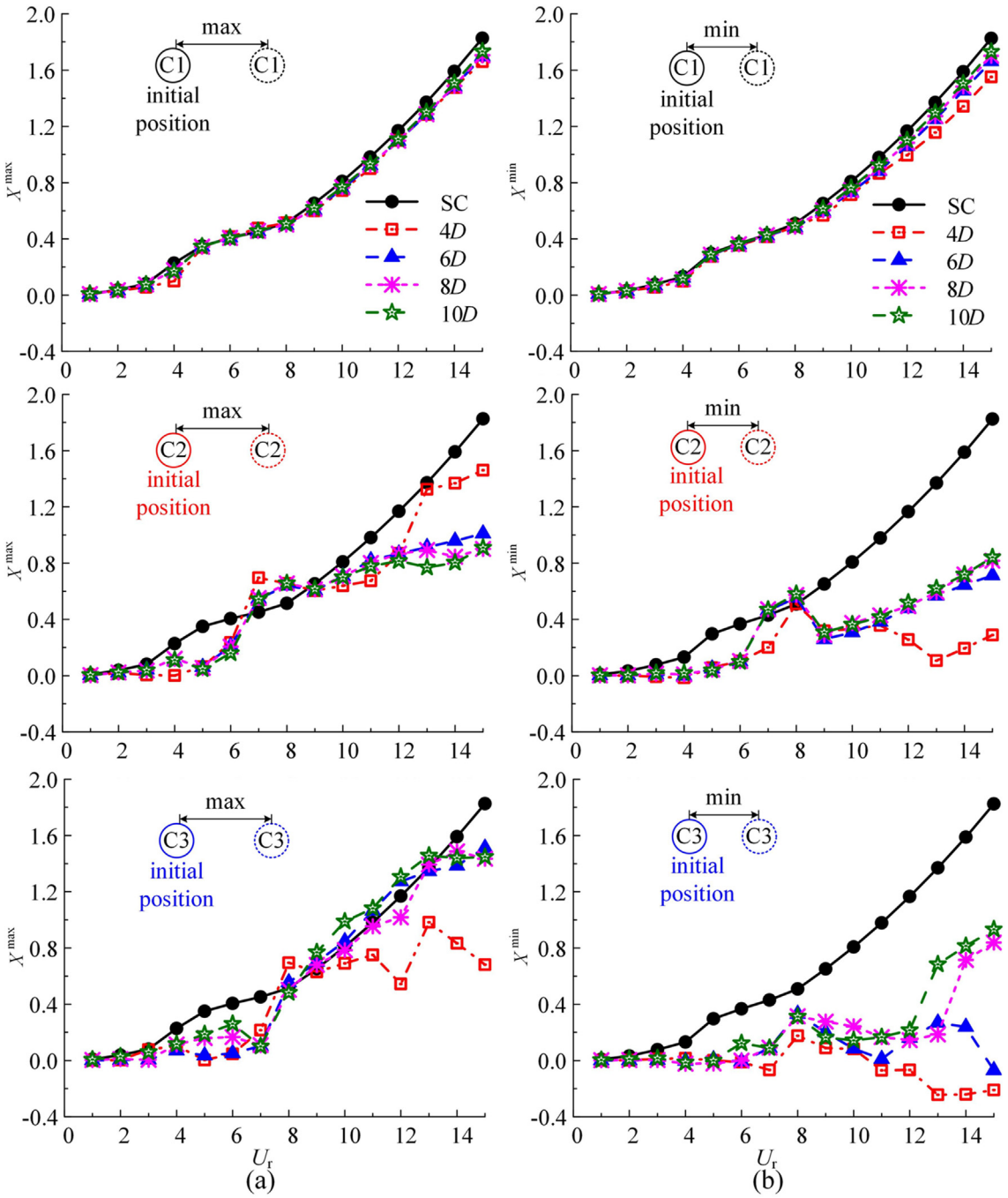

FIG. 9. The variation of the maximum and minimum values of the streamwise displacement: (a) the maximum value; (b) the minimum value.

In accordance with these definitions, it can be computed that the maximum streamwise displacement of the isolated cylinder is $X^{max} = 1.83$ and occurs at $U_r = 15$. It is also realized that the RMS value of the streamwise vibration of the upstream cylinder A_{x1}^{RMS} decreases after the VIV lock-in, except for the case of $L/D = 4$ in which the A_{x1}^{RMS} becomes as high as 0.05 for $U_r \geq 10$. On the other hand, the RMS value of the streamwise vibration of the middle cylinder A_{x2}^{RMS} changes significantly after $U_r = 6$ approximately. Meanwhile, the mean flow displacement of the middle cylinder *X*mean 2 is also found arising for $U_r = 6$–8. It is believed that this is directly caused by the transition between the wake interference regimes, as shown in Fig. 4. For $L/D = 4$ and $U_r \geq 8$, the wake interference regime of the cylinder C2 and the cylinder C3 changes from the QCS regime to the AR regime. It is also observed that the A_{x2}^{RMS} of the middle cylinder increases gradually for $U_r = 8$–11 and remains stable after $U_r \geq 13$. Furthermore, for the center-to-center spacing $L/D = 6$, 8, and 10, the A_{x2}^{RMS} of the middle cylinder is found decreasing gradually as well behind $U_r \geq 10$. Overall, it is found that the maximum streamwise displacement of the middle cylinder $X^{max} = 1.46$ occurs for $L/D = 4$ and $U_r = 15$, which is 20.22% lower than that of the isolated cylinder at $U_r = 15$. For the downstream cylinder beyond $U_r \geq 7$, the value of A_{x3}^{RMS} keeps increasing and the maximum vibration displacement $X^{max} = 1.51$ occurs for $L/D = 4$ and $U_r = 15$, which is 17.49% lower than those of the isolated cylinder at $U_r = 15$. In addition, the downstream cylinder presents the negative streamwise displacement, coinciding with the observation in previous literature.[26,27] The negative pressure between the middle and the downstream cylinders is the main reason, which will be confirmed in later.

The evolution of the instantaneous center-to-center spacing between the cylinders, L_{12} and L_{23}, during the vibration is also monitored in this study. Figure 10(a) shows that the time-averaged center-to-center spacing between the cylinder C1 and the cylinder C2, L_{12}^{mean}, slightly increases during $U_r = 6$–8. Thereafter, it starts decreasing as the reduced velocity exceed $U_r = 8$. For a high reduced velocity, for example, $U_r = 15$, the values of L_{12}^{mean}, respectively, are approximately 3.27, 5.18, 7.16, and 9.14 for the initial spacing 4, 6, 8, and 10. Overall, it is found that the value of L_{23}^{mean} decreases to 3.36 when the initial spacing is $L/D = 4$. On the other hand, the time-averaged center-to-center distance between the cylinder C2 and the cylinder C3, L_{23}^{mean}, gradually changes for the initial spacing $L/D = 6$, 8, and 10. Figure 10(b) shows that the value of L_{12}^{RMS}, the RMS of the instantaneous spacing between the cylinder C1 and the cylinder C2, and the value of L_{23}^{RMS}, the RMS of the instantaneous spacing between the cylinder C2 and the cylinder C3, also simultaneously follow the trend of A_{x2}^{RMS} in Fig. 8(b). It is also realized that the maximum value of L_{23}^{RMS} can reach as high as 0.84 in this study. The variation of the spacing ratio is closely related to the evolution of wake interference mode. Similar to the definitions of the streamwise vibration amplitudes, the statistical maximum and minimum streamwise spacing between cylinders can be expressed as

$$L^{max} = L^{mean} + \sqrt{2}L^{RMS}, \quad L^{min} = L^{mean} - \sqrt{2}L^{RMS}, \tag{8}$$

where L^{max} and L^{min} are the maximum and minimum spacing between cylinders, seen in Figs. 10(c) and 10(d). Based on these definitions, when the initial spacing is $L/D = 4$, the value of L_{12}^{max} can be obtained as 4.26 and occurring at $U_r = 7$, which is 6.5% above the initial spacing. On the other hand, the value of L_{12}^{min} can be obtained as 2.70 at $U_r = 15$, which is 32.5% lower than the initial spacing instead. By contrast, the maximum instantaneous spacing between the cylinder C2 and the cylinder C3 can be obtained as $L_{23}^{max} = 4.84$ and occurring at $U_r = 13$, which is 21.0% higher than the initial spacing. Similarly, the minimum instantaneous spacing between the cylinder C2 and the cylinder C3 can be computed as $L_{23}^{min} = 2.41$ is recorded at $U_r = 15$ and 39.75% lower than its initial spacing.

For the flow over three vibrating tandem cylinders, the instantaneous center-to-center spacing between the cylinders is a key parameter determining the wake interference regime, especially when the initial spacing is small. Figure 8 shows that the amplitudes of structural vibration are generally intensified proportionally with the increase in reduction velocity. Meanwhile, Fig. 10 also shows that the RMS values of the instantaneous center-to-center spacing also arise continuously with the increment of reduced velocity and result the transition between different wake interference regimes. For example, Fig. 11 illustrates the transition of the wake interference regime in time for $L/D = 4$ and $U_r = 7$. The time history of the streamwise displacement X of three tandem cylinders shows an irregular trajectory pattern that intermittently changes in time. The vorticity contours and pressure coefficient contours at few representative moments are also plotted in Fig. 11(b) for (1) $tU_\infty/D = 295.1$, (2) $tU_\infty/D = 313.5$, (3) $tU_\infty/D = 421.7$, and (4) $tU_\infty/D = 493.1$, respectively. Among them, it is obvious that the wake interference regime between the cylinder C1 and the cylinder C2 belongs to the AR regime, whereas the wake interference regime between the cylinder C2 and the cylinder C3 manifests a transition from the QCS regime to the AR regime and eventually changes back to the QCS regime at four instances in time. It is also noticed that the vortex structure behind the downstream cylinder retains the double-row vortex structure, although the vortex shedding of the downstream cylinder is inhibited in the QCS regime at the most of time. Therefore, it is classified as the AR–QCS regime based on the wake interference regime diagram in Fig. 4. In addition, the variations of vibration trajectories of three vibrating tandem cylinders at $L/D = 4$ and $U_r = 7$ during the transition between different wake interference regimes are shown in Fig. 11(c). It can be seen that before and after switching the wake interference modes, the vibration trajectories of the upstream cylinder exhibit a typical "8" shape, like the isolated cylinder, whereas the trajectories of the middle and the downstream cylinders show a "droplet" shape[27] and an "inverted droplet" shape, respectively. During the transition of wake interference regime, the wake interference modes of the cylinder C1 and the cylinder C2 are always the AR mode. As a result, the vibration response of the upstream cylinder can keep the typical "8" shape, but the trajectories of the cylinder C2 and the cylinder C3 are significantly changed and resulted in the mode switching. The different vibration trajectories also significantly influence the wake dynamics and the associated pressure distribution in wake. Figure 11(b) shows the pressure coefficient contour in the wake behind three vibrating cylinders. It can be found that the pressure fluctuation around the surface of downstream cylinder is small and exhibits the characteristics of the AR model, in which the vortices detach from the middle cylinder alternately and re-attach to the downstream cylinder's surface. It results in a large structure vibration of the downstream cylinder during the mode switching between different wake interference regimes.

The structural dynamics during VIV lock-in can be further classified into three distinction branches: the initial branch (IB), the lower

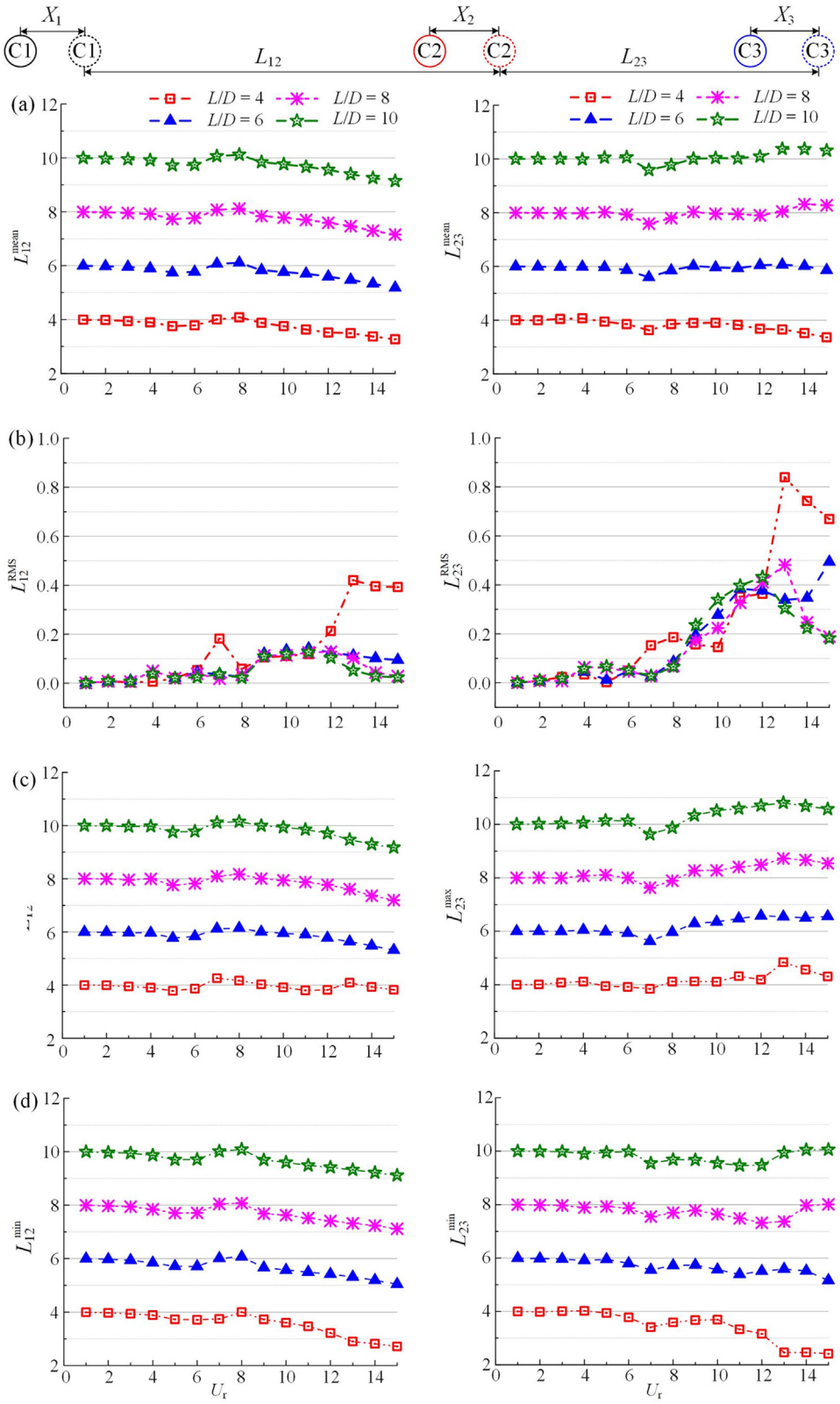

FIG. 10. Variation of the center-to-center spacing: (a) the time-averaged spacing (L_{12}^{mean} and L_{23}^{mean}); (b) the root-mean-squared value of spacing (L_{12}^{RMS} and L_{23}^{RMS}); (c) the maximum value of spacing (L_{12}^{max} and L_{23}^{max}); (d) the minimum value of spacing (L_{12}^{min} and L_{23}^{min}).

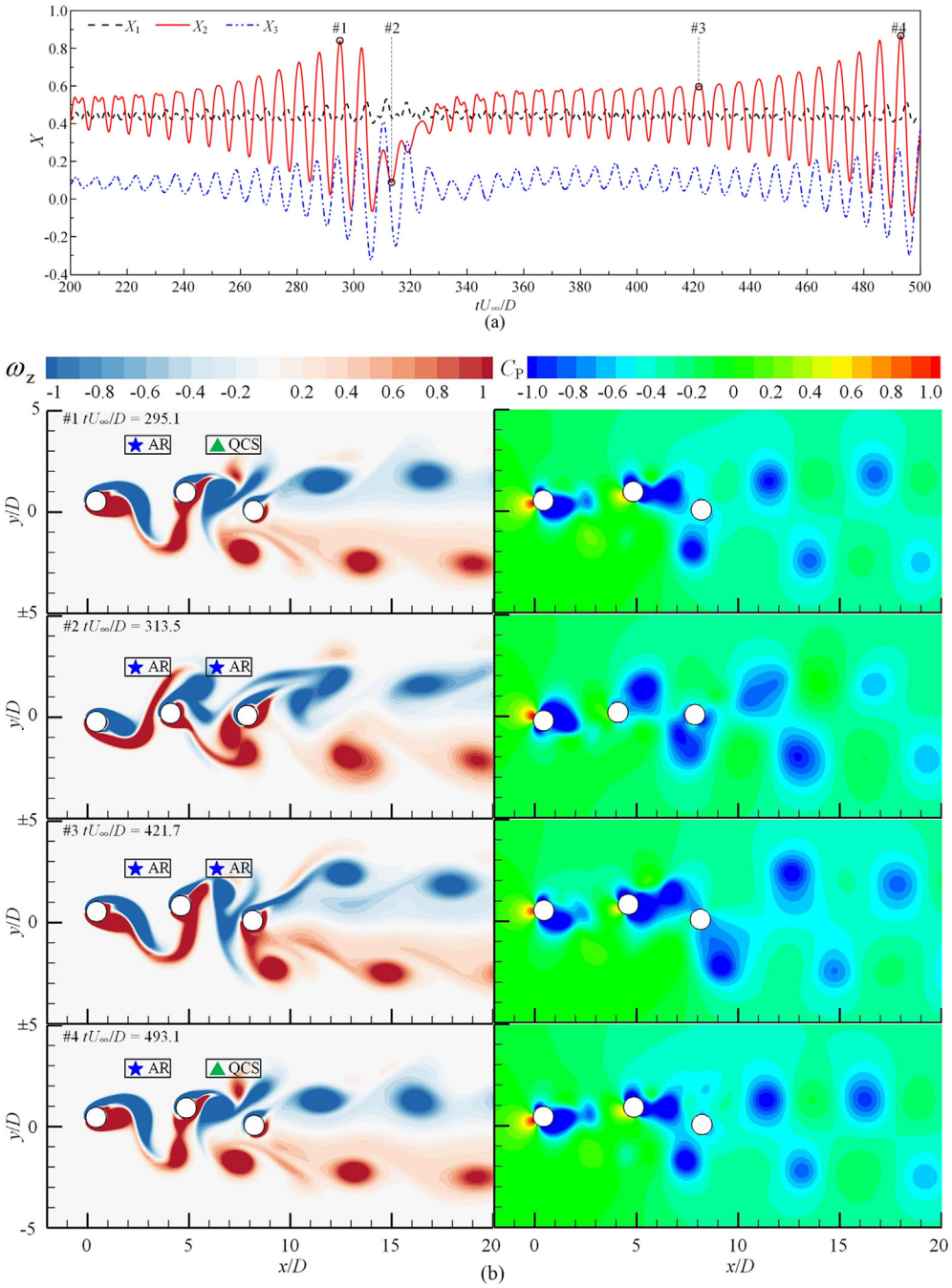

FIG. 11. The switching of wake interference mode over time at $L/D = 4$, $U_r = 7$, and $tU_\infty/D = 200$–500: (a) streamwise displacements of three tandem cylinders; (b) vorticity (ω_Z) and pressure coefficient (C_P) contours at four representative moments; (c) vibration trajectories of three tandem cylinders during the transition between different wake interference modes.

branch (LB), and the desynchronization branch (DB).[47] In this study, it shows that the upstream cylinder in tandem arrangement also exhibits the typical IB, LB, and DB branches of VIV lock-in and these branches also agree well with the results previously reported for the isolated vibrating cylinder previously. Based on the transverse vibration amplitudes in Fig. 12, it can be seen that both the isolated cylinder and the upstream cylinder show a similar VIV lock-in response within the range of $U_r = 5$–7. For example, as shown in Fig. 12(a), the value

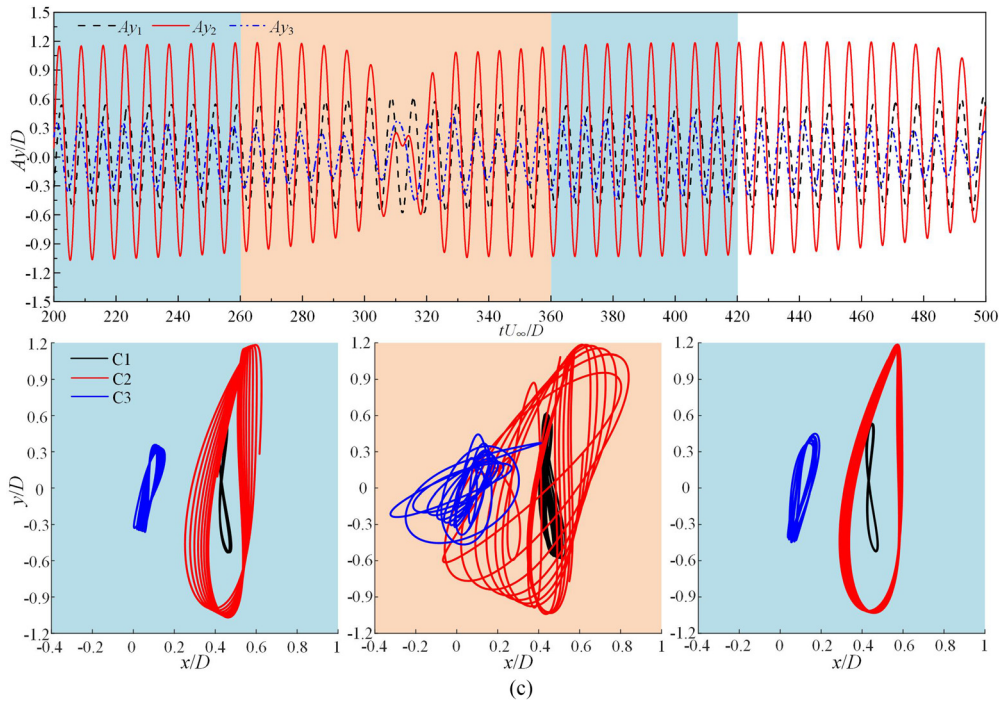

FIG. 11. (*Continued.*)

of A_y^{RMS} of the upstream cylinder shows a typical VIV response and is similar to the response of an isolated vibrating cylinder. It is also further noticed that the IB branch is within the range $U_r = 1$–4, and the LB branch falls in the range $U_r = 5$–7 and the DB branch occurs at $U_r = 8$–15 for the upstream cylinder in tandem arrangement. In addition, the corresponding VIV lock-in phenomenon is highlighted in yellow color in the frequency domain, as shown in Fig. 12(b). In addition, it is also evident that the structural dynamics of each cylinder is significantly different from each other. Especially, the maximum transverse fluctuation of both cylinder C2 and C3 is significantly large than that of the upstream cylinder in Fig. 12(a). It is also noticed that the onset of VIV lock-in of the upstream cylinder occurs at a relatively higher reduced velocity value $U_r = 4$ and, similarly, the end of the VIV lock-in also appears at a higher reduced velocity value $U_r = 9$. As the corresponding VIV lock-in range expands, the upstream cylinder switches to the de-synchronization branch for $U_r = 9$–15. It is known that the frequency of transverse vibration is locked to the natural frequency of structure $f_{Ay1}/f_n = 1$ during VIV lock-in. Therefore, this switch of VIV lock-in to a higher reduced velocity value for the upstream cylinder can be clearly confirmed in Fig. 12(b). Furthermore, the values of A_{y1}^{RMS} for the upstream cylinder at different spacing values are slightly higher than those of the isolated cylinder after $U_r > 4$ instead.

Because both the middle and downstream cylinders are immersed in the wake behind the upstream cylinder, the structural dynamics is severely perturbed by the strong shear layers and shed vortices from the upstream cylinder. Hence, the corresponding structure instability of the middle and downstream cylinders in fluid was classified as the wake-induced vibration (WIV) in the literature. As shown in Fig. 12(a), the onset of VIV lock-in for the middle cylinder is excited beyond $U_r = 5$. This is generally true for all center-to-center spacing analyzed in this study, for example, $L/D = 4$, 6, 8, and 10 in Fig. 12(a). Therefore, the initial branch of the vibration for the middle cylinder is defined as $U_r = 1$–5. As the reduced velocity increases further $U_r = 6$–8, the frequency of the transverse vibration of the middle cylinder is locked to $f_{Ay2}/f_n = 1$. Following that, $U_r = 9$–12 becomes the desynchronization branch of the vibration for the middle cylinder. However, as the reduction velocity continues increasing, the frequency of the transverse vibration of the middle cylinder shows a drop phenomenon for $U_r > 12$. This is same to the observation recorded by Zhu *et al.*,[46] in which as the value of A_{y2}^{RMS} increases for the middle cylinder and the wake-induced galloping WIG occurs on the middle cylinder. When the spacing ratios are $L/D = 6$, 8, and 10, it can be seen from the trend of A_{y2}^{RMS} values of the middle cylinder that the structural dynamics of the middle cylinder enters the desynchronization branch within the range $U_r = 9$–10. Furthermore, it is also found that the vibration frequency of the middle cylinder becomes locked to the structural frequency, $f_{Ay2}/f_n = 1$ for $L/D = 10$ and $U_r = 5$–12. By contrast, the vibration frequency of the middle cylinder keeps desynchronizing the mode switching process for $L/D = 6$, 8, and 10, and $U_r = 12$ and 13, respectively. As shown in Fig. 12(b), compared with the lower branch and the VIV lock-in stage of the isolated vibrating cylinder for $U_r = 5$–7, the lower branch and VIV lock-in stage of the downstream cylinder in tandem arrangement are found delayed to much higher reduced velocity values $U_r > 8$.

In addition, it is found that the lock-in regime ($f_{Ay1}/f_n \approx 1$) of the upstream cylinder expands to $U_r = 5$–8, similar to the

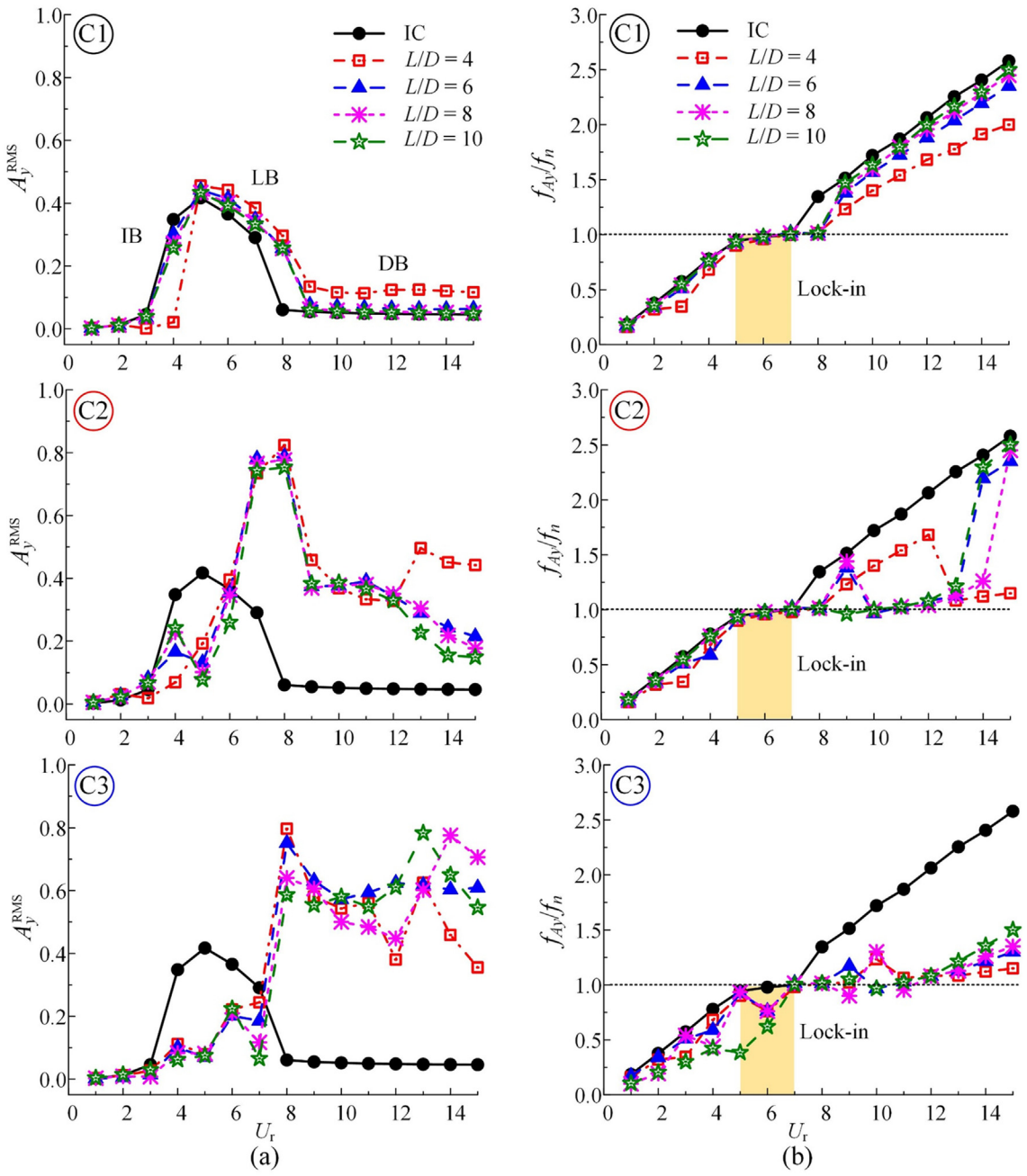

FIG. 12. Transverse vibration response of three tandem cylinders: (a) root-mean-squared (RMS) transverse amplitudes (A_y^{RMS}); (b) the normalized frequencies of transverse vibration (f_{Ay}/f_n), where the VIV lock-in of an isolated cylinder is highlighted in yellow color.

observation in Gao *et al.*[26] For the middle cylinder with the initial spacing ratio of $L/D = 10$, the transverse vibration is in the lock-in regime ($f_{Ay2}/f_n \approx 1$) at $U_r = 5$–8 and switches to the de-synchronization branch at $U_r = 9$–12. It is interesting to find the response returns to the lock-in regime around $U_r = 13$–15, termed the secondary lock-in. This phenomenon has been found in the vortex-induced vibration of a cylinder subject to cross buoyancy.[35] When $L/D = 6$, the secondary lock-in appears at $U_r = 10$–13 for the middle cylinder. When $L/D = 8$, the secondary lock-in range is extended to $U_r = 10$–14, whereas this secondary lock-in disappears for $L/D = 10$, and the first lock-in regime expands to $U_r = 5$–13. The normalized frequency of the downstream cylinder undergoes

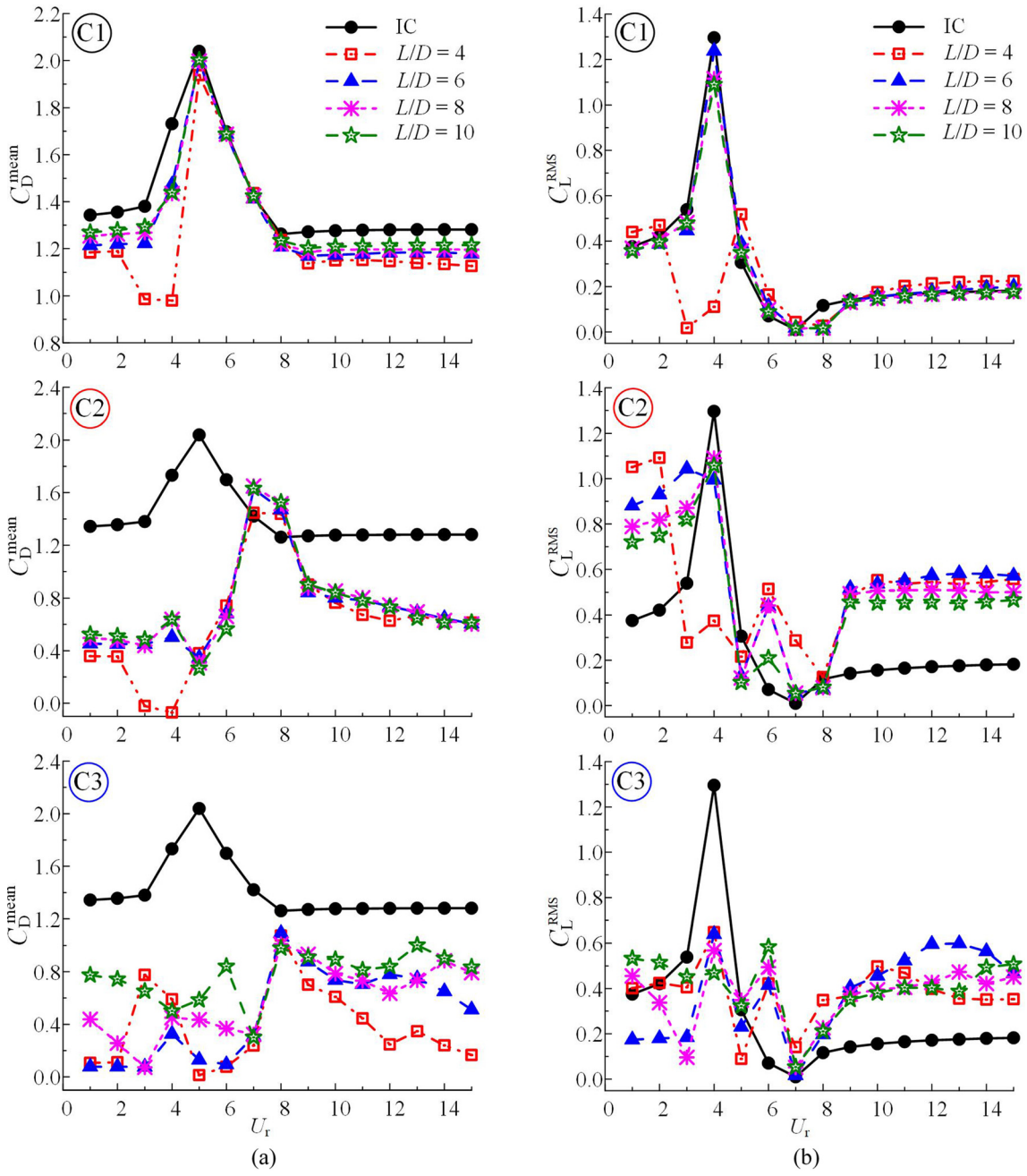

FIG. 13. Variation of hydrodynamic coefficients vs the reduced velocity: (a) the time-averaged drag coefficient (C_D^{mean}); (b) the root-mean-squared lift coefficient (C_L^{RMS}).

sharp drop and rise in the range of $U_r = 6$–12, due mainly to the irregular response.[26]

C. Hydrodynamic coefficients

Figure 13 shows the comparison of hydrodynamic coefficients of the three tandem cylinders against those of an isolated cylinder. The time-averaged drag coefficient (C_D^{mean}) and the root-mean-squared lift coefficient (C_L^{RMS}) are defined as

$$C_D^{mean} = \frac{1}{N}\sum_{i=1}^{N}\frac{h_x^{*cyl}}{0.5\rho_0 U_\infty^2 D}, \quad C_L^{RMS} = \sqrt{\frac{1}{N}\sum_{i=1}^{N}\left[\frac{h_y^{*cyl}}{0.5\rho_0 U_\infty^2 D}\right]^2}, \quad (9)$$

where N is the number of values in the time series for statistics, h_x^{*cyl} and h_y^{*cyl} are the dimensionless fluid and structural stresses along with the fluid–structure interface, respectively. For the vortex-induced vibration of an isolated cylinder, the mean drag coefficient C mean D

increases proportionally within $U_r = 1$–5, the initial branch (IB), as shown in Fig. 13(a). Subsequently, its value becomes decreasing within the range $U_r = 5$–8, which is defined as the lower branch (LB) of VIV instead. Following that, the region within $U_r = 9$–15 is referred to as the desynchronization branch (DB). Similar to the characteristics of drag coefficients, it is also found that the RMS amplitude of lift coefficient C_L^{RMS} of the isolated cylinder increases during the initial branch ($U_r = 1$–4) and decreases in the low branch ($U_r = 4$–7) in Fig. 13(a). Thereafter, the value of C_L^{RMS} starts increasing again within the desynchronization branch ($U_r = 7$–15). Compared with vortex-induced vibration of the isolated cylinder, the values of C_{D1}^{mean} and C_{L1}^{RMS} of the upstream cylinder vary simultaneously with the value of U_r, except for the reduced velocity range $U_r = 6$–8 within which the fluctuation of lift force is almost suppressed for all L/D values. It is observed that they rise within the initial branch, which is $U_r = 1$–5 for the upstream cylinder, and decrease within the lower branch ($U_r = 5$–9) instead. By contrast, their values retain unchanged for the desynchronization branch ($U_r = 9$–15). Nonetheless, their overall values are still slightly lower than the hydrodynamic coefficient of an isolated cylinder. In addition, it is noticed that the mean drag coefficient of upstream cylinder C_{D1}^{mean} for $L/D = 4$ and $U_r = 3$–4 becomes much smaller than the other cases having a greater spacing ratio and the same U_r values. It is believed that this is attributed to its wake interference mode. As shown in Figs. 4 and 5, the shear layers from the upstream cylinder no longer shed into vortices downstream but re-attach to the downstream cylinder (the CR regime), results in a significantly narrower wake behind the upstream cylinder, since the value of C_{D1}^{mean} reduces obviously. The RMS value of the lift coefficient for the upstream cylinder C_{L1}^{RMS} is found smaller within the range of $U_r = 3$–4, because of the continuous reattachment (CR) regime between the cylinder C1 and the cylinder C2. In this case, the position of vortex formation is relatively longer in the alternate reattachment (AR) mode, because of the strong kinetic energy injected by the separated shear layers of the upstream cylinder. Since the wake of the upstream cylinder does not belong to the continuous reattachment (CR) mode, the trend of the value of C_{L1}^{RMS} follows the characteristics of the other regimes.

For the middle cylinder, Fig. 13 also shows that the variation of its C_{D2}^{mean} and C_{L2}^{RMS} values compared with those of the isolated vibrating cylinder. It is noticed that the C_{D2}^{mean} values of the middle cylinder are generally much lower than those of the isolated cylinder, except for the reduced velocity range $U_r = 7$–8, since the value of C_{D2}^{mean} is mainly affected by the width of wake of the middle cylinder. It is surprised to observe that the time-averaged drag coefficient of the middle cylinder C_{D2}^{mean} is less than zero for $L/D = 4$ and $U_r = 3$–4. It is believed that these negative drag forces originate from the formation of a large low-pressure recirculation region in the gap between the upstream cylinder and downstream cylinder, where the shear layers of the upstream cylinder steadily re-attach to the surface of the middle cylinder in the CR mode. The values of C_{L2}^{RMS} of the middle cylinder are remarkably different from that of the isolated cylinder because of the disturbance imposed by both the upstream cylinder and the downstream cylinder. The separated shear layers from the upstream cylinder significantly inhibit the vortex shedding process of the middle cylinder for $L/D = 4$ and $U_r = 3$–4 and results in very low C_{L2}^{RMS} values. Except for the VIV lock-in ($U_r = 5$–8 in this case) in Fig. 13(a), the C_{L2}^{RMS}values of the middle cylinder are generally small, but still higher than that of the isolated cylinder. The co-shedding (CS) mode is observed behind the middle and downstream cylinders for the high reduced velocity values.

It is further noticed that the time-averaged drag coefficient of the downstream cylinder C_{D3}^{mean} is significantly influenced by the wake-induced vibrations of its neighboring cylinders for the different L/D and U_r values, as shown in Fig. 13. The shear layers separate from the middle cylinder and re-attach to the downstream cylinder for $L/D = 4$ and $U_r = 3$–4. Its wake interference regime evidently switches from the QCS mode to the AR mode and results in an increased C_{D3}^{mean} value of the downstream cylinder. In addition, the downstream cylinder exhibits a wake-induced galloping state for $U_r = 8$, which causes a decrease in C_{D3}^{mean} value of the downstream cylinder instead. Recollecting the classification shown in Fig. 4, it indicates that the wake interference between the cylinder C2 and the cylinder C3 belongs to the QCS mode for $L/D = 6$ and $U_r = 1$–3. In the QCS mode, the vortex shedding process behind the downstream cylinder is significantly inhibited and leads to the further decrease in the C_{D3}^{mean} values. Instead, for $U_r > 3$, the wake interference regime between the cylinder C2 and the cylinder C3 switches to the CS mode accordingly. As shown in Fig. 13, Within the range of $3 < U_r < 8$ (before the intensive vibration of the downstream cylinder), the decreased C_{D3}^{mean} values can be attributed to the presence of two kinds of vortical structures, for instance, the representative cases as shown in Fig. 6: first the vortical structure behind the middle cylinder manifests a 2S shedding mode for $U_r = 4$; however, a double-row vortical structure is observed around the middle cylinder for $U_r = 5$ and 6, instead. Consequently, the presence of the double-row vortex overtly inhibits the vortex shedding process of the downstream cylinder and results in a decrease in C_{D3}^{mean} values.

As the center-to-center spacing increases further, for example, $L/D = 8$, based on the classification in Fig. 4, the wake interference mode between the cylinder C2 and the cylinder C3 becomes the QCS mode for $U_r = 1$–3. It is believed that this is attributed to the detached double-row vortex structure and the formed secondary vortices downstream, for example, the representative cases in Fig. 7. It is found that the secondary vortex is formed behind the downstream cylinder at $U_r = 3$ and causes a linear decrease in the C_{D3}^{mean} values. By contrast, the shed vortex clusters behind the middle cylinder form isolated vortical structures for $U_r > 3$ instead and induce the 2S vortex shedding mode downstream the downstream cylinder. The values of C_{D3}^{mean} increase gradually until the downstream cylinder enters the galloping mode for $U_r < 8$. For a much larger initial spacing $L/D = 10$, the vorticity contour plot of the exemplary case in Fig. 7 shows that a double-row vortex structure is formed around the middle cylinder and coalesces downstream to form the secondary vortices and lead to a decrease in the pressure difference between the cylinder C2 and the cylinder C3. As a result, the values of C_{D3}^{mean} decrease slightly for $U_r = 4$. Within the range $U_r = 4$–7, the dynamics of the downstream cylinder is similar to the isolated cylinder, in which the VIV lock-in state abruptly changes from the initial branch to the lower branch and subsequently the wake galloping state.

Figure 14(a) shows the variation of the dominant frequency of lift coefficient $f_{C_{Ld}}^*$ of the isolated cylinder and three vibrating tandem cylinders against the reduced velocity. In regard to the isolated vibrating cylinder, its $f_{C_{Ld}}^*$ values increase by 0.025 until the onset of VIV lock-in ($U_r = 1$–4) and decrease rapidly by 0.08 until the end of VIV lock-in ($U_r = 5$–7). After VIV lock-in, its value remains at a constant value inside the desynchronization branch

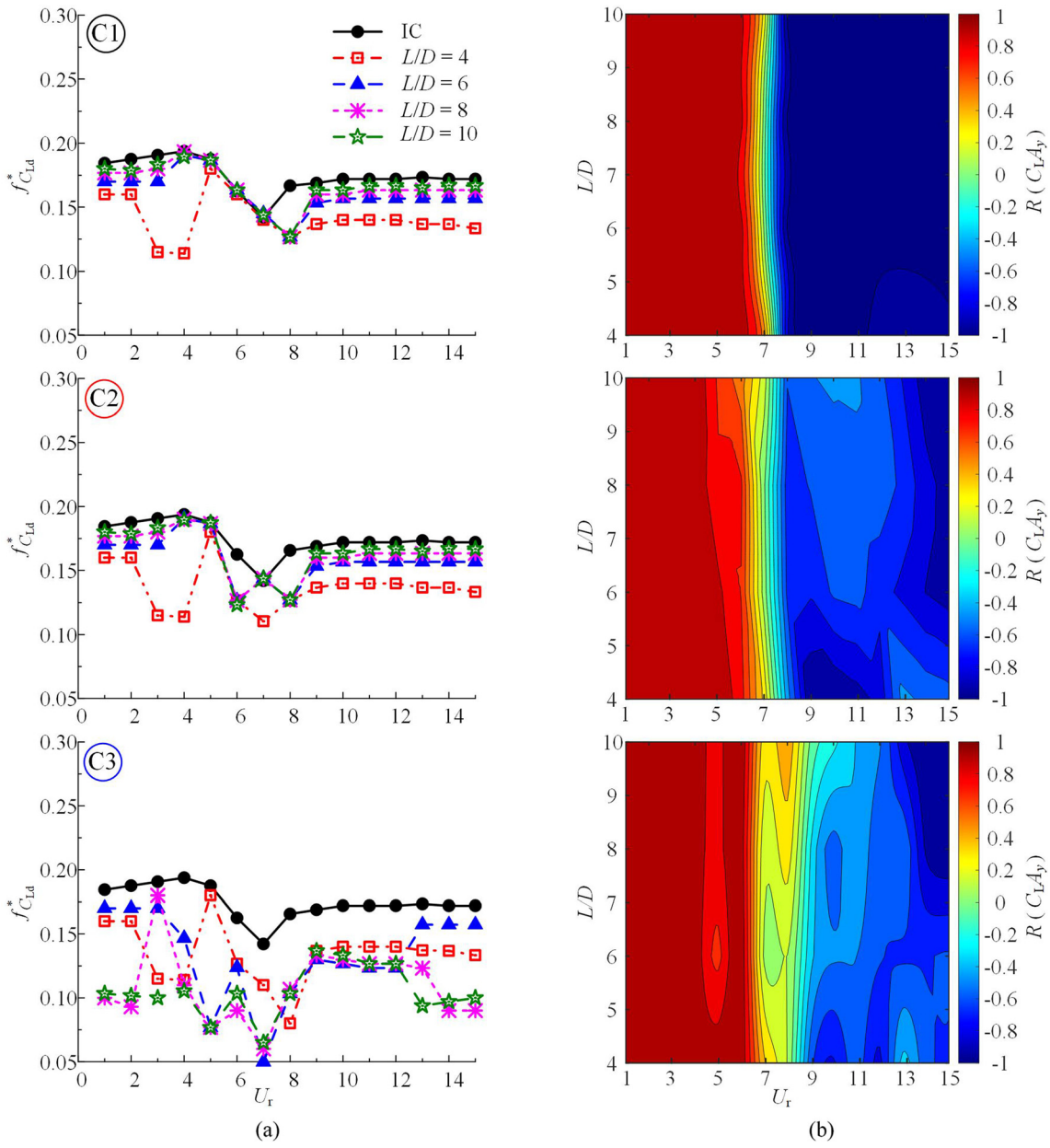

FIG. 14. Frequency of lift coefficient and its correlation with the crossflow amplitude: (a) the dominant frequency of lift coefficient ($f^*_{C_{Ld}}$) against U_r; (b) correlation coefficient between the lift coefficient and transverse amplitude.

($U_r = 8$–15). Figure 14(a) also shows that there is a significant reduction of $f^*_{C_{Ld}}$ values of all three vibrating tandem cylinders for $L/D = 4$ and $U_r = 3$–4. For the upstream and downstream cylinders, their values of $f^*_{C_{Ld}}$ are very close to those of an isolated vibrating cylinder for the ranges of reduced velocity and spacing ratios in this study. By contrast, the $f^*_{C_{Ld}}$ values of the downstream cylinder show lots of variations for different reduced velocity and spacing ratios, compared with those of an isolated vibrating cylinder. Overall, it is found that the $f^*_{C_{Ld}}$ values of the downstream cylinders in call cases are much smaller than those of an isolated vibrating cylinder, due to wake-induced disturbance imposed by the upstream and middle cylinders.

In this study, the Pearson correlation coefficient (R), as defined in Eq. (10), is employed to quantify the linear correlation/dependency between the variables, for instance, the lift force and the transverse vibration amplitude

$$R(C_L, A_y) = \frac{\mathrm{cov}(C_L, A_y)}{\sqrt{\mathrm{Var}[C_L]\mathrm{Var}[A_y]}}, \tag{10}$$

where cov () is the covariance of two variables, and Var [] is the variance of a variable. In this study, the Pearson correlation coefficient is used to determine the phase angle difference (Φ) between the lift force and the transverse vibration amplitude. When $R(C_L, A_y) = 1$, C_L and A_y are in the same phase $\Phi = 0°$; when $R(C_L, A_y) = -1$, the reverse phase is of C_L and A_y $\Phi = 180°$. Whereas when $-1 < R(C_L, A_y) < 1$, it is believed that the C_L is out of phase with A_y. Figure 14(b) shows that the $R(C_{L1}, A_{y1})$ of the upstream cylinder has a phase difference $\Phi \leq 90°$ for $U_r < 7$ and $\Phi > 90°$ for $U_r > 7$. It is also noticed in Fig. 14(b) that the $R(C_{L2}, A_{y2})$ of the middle cylinder and the $R(C_{L1}, A_{y1})$ of the upstream cylinder vary simultaneously, whereas the phase difference of the downstream cylinder $R(C_{L3}, A_{y3})$ retains $\Phi \leq 90°$ for $U_r < 7$ and $\Phi > 90°$ for $U_r > 8$.

D. Influence of structural dynamics on heat convection

In forced convection flow, the transport of thermal energy is completely driven by fluid inertia in wake. As shown in Fig. 15, the four fundamental regimes classified in Fig. 4 are also observed. For three vibrating tandem cylinders, these fundamental wake interference regimes can be further categorized into six different combinations of these regimes, for example, the AR–QCS, CR–AR, AR–AR, CS–QCS, CS–CS, and AR–CS modes in Fig. 15, to account for the mutual interference between vibrating cylinders.

Figure 16 shows that the results of thermal convection over three vibrating tandem cylinders for different values of spacing ratios and reduced velocity. It is found that the variations of the Nu^{mean} and Nu^{RMS} values of each cylinder with against the reduced velocity are strongly correlated with characteristics of C_D^{mean} against the reduced velocity shown in Fig. 13(a), except for the cases showing the CR wake interference mode for $L/D = 4$ and $U_r = 3$–4. Especially, the Nu^{RMS} values of each cylinder are intimately related to the dynamics of lift force as well.

To explore the correlation between the structural dynamics and the transport of thermal energy in fluid, the results are projected into the frequency domain for better observation of their eigen-spectrum. The wavelet scalogram is an illustration of a signal in frequency–time domain. In this study, it is used to explore the relationship between heat convection over the cylinders (Nu) and the associated hydrodynamic forces. Both the real-valued (Mexican hat) and the complex-valued (Gabor and Morlet) wavelets are generally employed for analysis. Compared with its counterpart, Gabor wavelet, the Mexican hat wavelet provides a relatively high resolution in the time domain and a coarse resolution in the frequency domain. On the contrary, the Morlet wavelet renders a higher resolution in the frequency domain and a coarser resolution in the time domain than the Gabor wavelet. The real-valued wavelet isolates the local minima and maxima of a signal. When the resolution of frequency is important, the Gabor wavelet can be used to plot the real part of the wavelet analysis and trace the minima and maxima of a signal.[32] Depending on the nature of the signal and its intrinsic characteristics, one can choose a suitable mother wavelet. Therefore, the Gabor wavelet is chosen in this study. The time histories of C_D, C_L, and Nu values of an isolated vibrating cylinder in forced convection are plotted in Fig. 17 as the referential values for the subsequent comparison with three tandem cylinders. Their contours of the continuous wavelet transform and the fast Fourier transform of C_D, C_L, and Nu are also presented in Fig. 17.

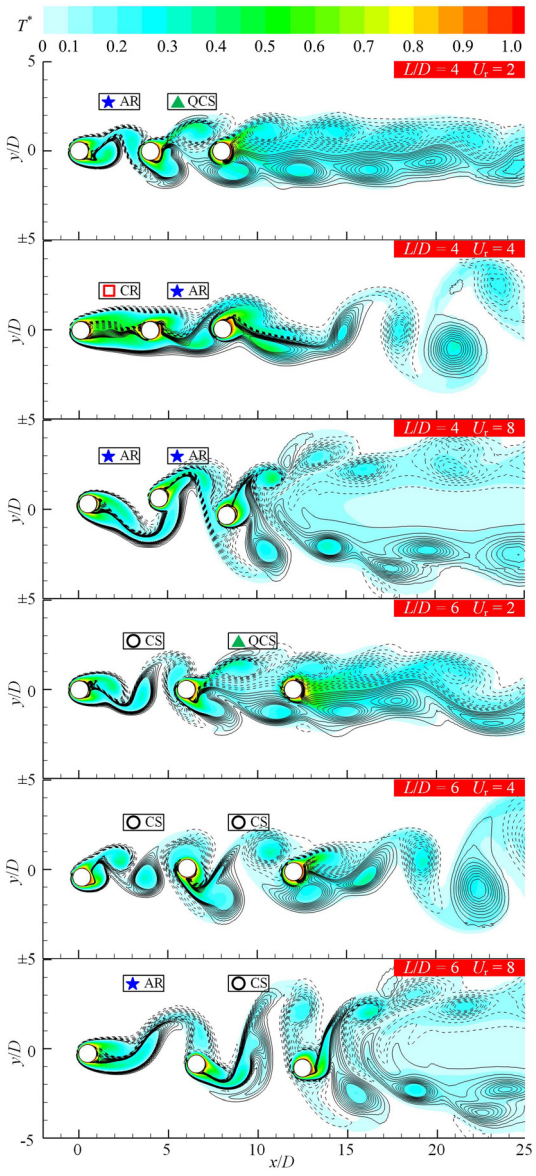

FIG. 15. Comparison of the vorticity and temperature contours for the three tandem cylinders in different wake interference modes.

The alternate appearance of the peak and root values in the wavelet scalogram represents the existence of the maximum and minimum values of C_D, C_L, and Nu, respectively. Figure 17 shows that the frequencies obtained by the continuous wavelet transform are the same as those obtained by fast Fourier transform. By comparing the continuous wavelet transform cloud images of C_D, C_L, and Nu in Fig. 17 at $U_r = 5$, it is found that the heat convection over an isolated cylinder is primarily driven by the drag force, since $f^*_{C_D} = f^*_{Nu} \approx 2f^*_{C_L}$. Meanwhile,

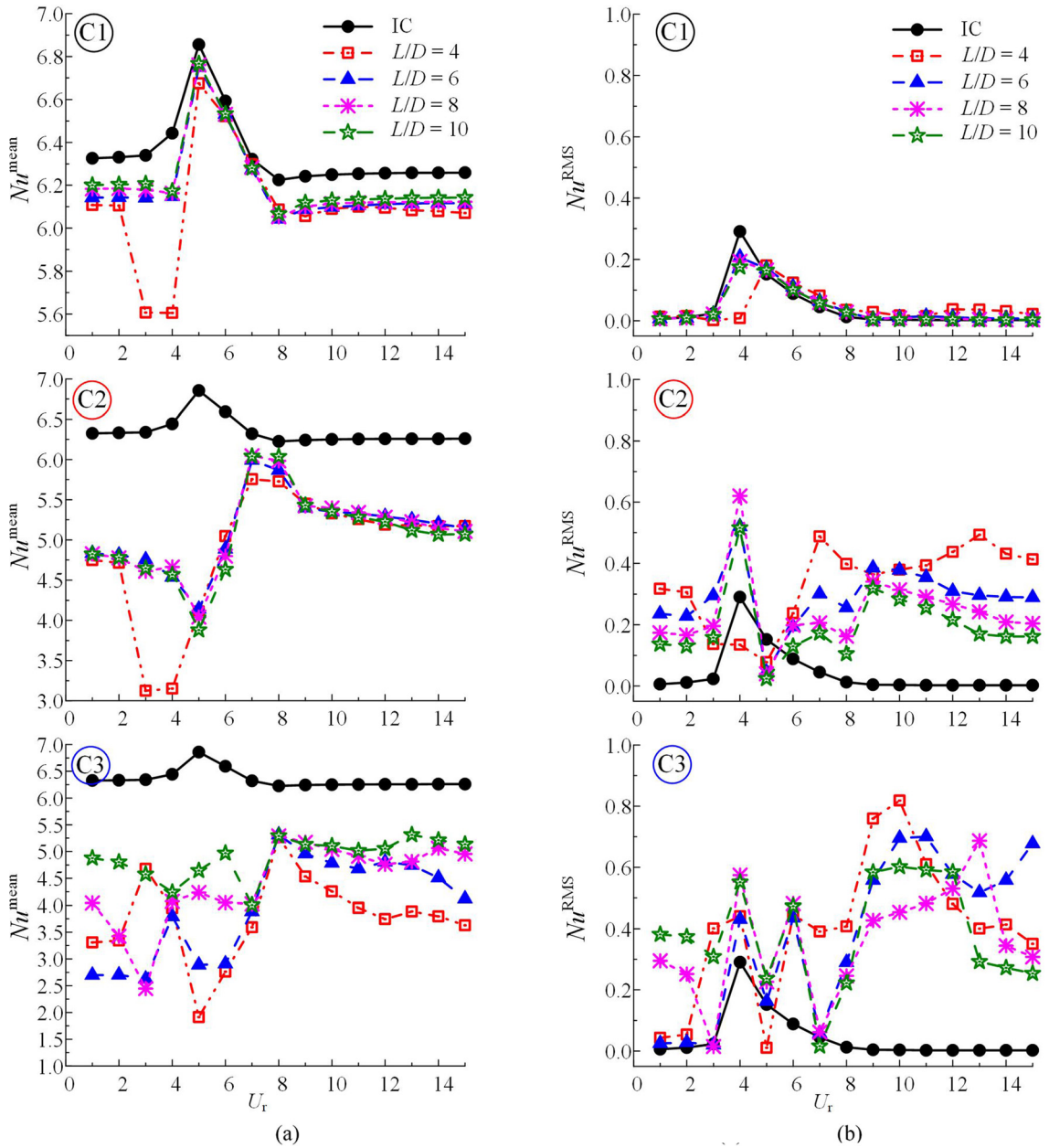

FIG. 16. Variation of the Nusselt number against U_r: (a) the time-averaged Nusselt numbers (Nu^{mean}); (b) the root-mean-squared Nusselt numbers (Nu^{RMS}).

the wake interference mode between the cylinder C2 and the cylinder C3 also changes from the QCS mode to the AR mode, as shown by the mode classification in Fig. 4 and the representative contour plots in Fig. 5.

The time histories of C_D, C_L, and Nu and the continuous wavelet transform of three vibrating tandem cylinders in Fig. 18 belong to the cases of $L/D = 4$, $tU_\infty/D = 300$–400, and U_r=6, 8. For the upstream cylinder, Fig. 18 shows that the dominant frequencies of C_D, C_L, and Nu are always decreasing and the energy is more dispersed. For $U_r = 8$, both the continuous wavelet transform and the fast Fourier transform of the upstream cylinder's lift force show that there is a third frequency phenomenon. Moreover, it still satisfies the relationship: $f^*_{C_D} = f^*_{Nu} \approx 2f^*_{C_L}$. The continuous wavelet transform cloud image in Fig. 18(b) shows that the middle cylinder is dominated by the drag force $f^*_{C_D} \approx f^*_{Nu}$, but there are many harmonics. The third frequency of the upstream cylinder C_L is amplified on the middle cylinder for $U_r = 8$, while the wake interference modes of the upstream, middle, and downstream cylinders are always in the AR mode. In addition, it is

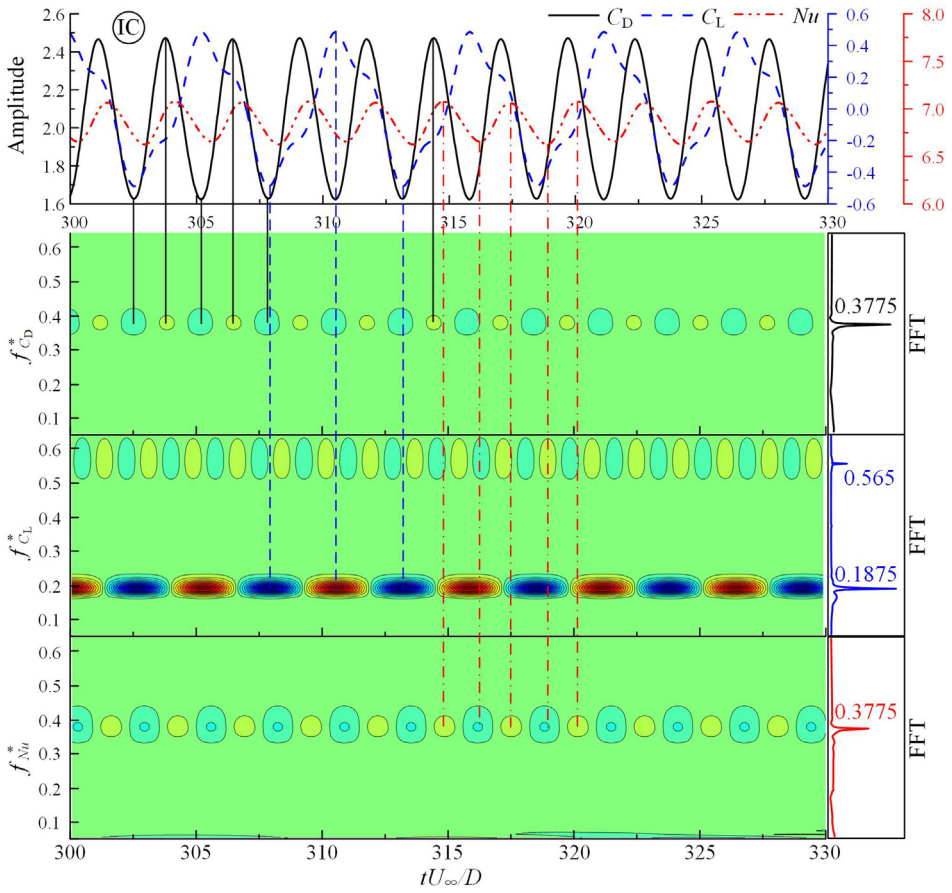

FIG. 17. Time histories of C_D, C_L, and Nu and associated frequency contours of an isolated cylinder at $U_r = 5$.

also found that the frequency spectrum of heat convection (Nusselt number) over the middle cylinder shows multiple modes, for example, 2 and 1/2 times of the fundamental frequency. As a result, the $f^*_{C_D} \approx f^*_{Nu} \approx 2f^*_{C_L}$ relationship is getting weaker for the middle cylinder. On the other hand, the downstream cylinder exhibits a number of complex physical phenomena. It is realized that the downstream cylinder exhibits the QCS wake interference mode, while its vortex formation is found suppressed. In regard to the hydrodynamic forces of the downstream cylinder, the frequency of lift coefficient C_L is found similar to that of the middle cylinder and the bandwidths of C_D and Nu frequency increase significantly. Furthermore, the heat convection (Nusselt number) of the downstream cylinder is found dominated by the drag force as well. For $U_r = 8$, both the middle and downstream cylinders exhibit the AR wake interference mode. As typical characteristics of AR mode, the frequency of lift coefficient C_L is close to that of the middle cylinder, but the frequency bandwidths of C_D, C_L, and Nu increase significantly instead. In addition, the heat convection rate over the downstream cylinder is also affected by the lift force as well.

Compared with three tandem cylinders, the wake structure of an isolated cylinder develops freely without interference. In one cycle of lift coefficient, two vortices are alternately shed from the cylinder surface, resulting in $f^*_{C_D} = f^*_{Nu} = 2f^*_{C_L}$ and the figure-eight orbit. A_y^{RMS} of the middle and downstream cylinders is smaller than that of an isolated cylinder at low reduced velocities ($U_r < 7$), and the associated vortices are influenced by those shed from the upstream cylinder surface, leading to $f^*_{C_D} = f^*_{Nu} \approx 2f^*_{C_L}$ for each cylinder. By contrast, the responses of the middle and downstream cylinders become irregular and aperiodic at high reduced velocities ($U_r > 7$), due to the enhanced wake interference.[25,26] With the increase in transverse amplitude, the time-averaged Nusselt number (Nu^{mean}) increases accordingly, seen in Fig. 16. In addition, during the oscillation, the thermal boundary layer separated from the upstream cylinder affects the associated separation of middle and downstream cylinders, contributing to the fluctuation of lift coefficient and harmonics. As reported by Zafar and Alam,[48] the vortex impingement introduces ambient cold fluid into the cylinder thermal boundary layer. Therefore, the fluctuation frequency of Nu for the middle and downstream cylinders is obviously affected by the lift coefficient.

IV. CONCLUSIONS

In this study, the flow-induced vibration and heat convection of three isothermal cylinders in forced convection were numerically investigated at low Reynolds number ($Re = 150$) for $Pr = 0.71$ and $1.0 \le U_r \le 15.0$. The center-to-center spacing ratio between cylinders varied between $4.0 \le L/D \le 10.0$. The wake interference regimes were classified into four fundamental wake interference modes over the range of reduced velocity in this study. Six different combination modes of these wake interference regimes, AR–QCS, CR–AR, AR–AR,

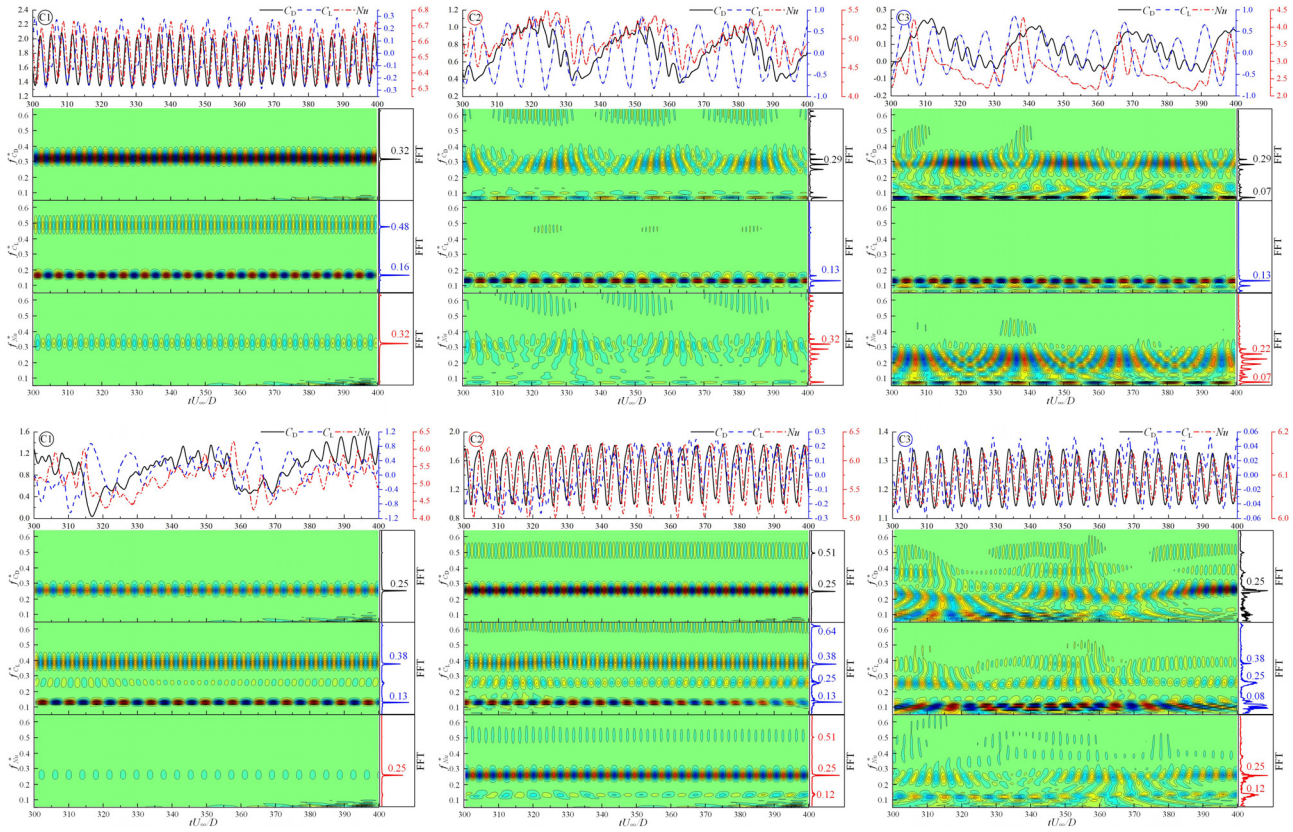

FIG. 18. Correlation between hydrodynamic coefficients and the heat transfer of the three cylinders in tandem with $L/D = 4$: (a) time histories of C_D, C_L, and Nu and associated frequency contours at $U_r = 6$; (b) time histories of C_D, C_L, and Nu and associated frequency contours at $U_r = 8$.

CS–QCS, CS–CS, and AR–CS, were identified in the numerical results of flow-induced vibration and heat convection. The comparison has shown that the dynamics of thermal energy transfer was driven by the vortex dynamics in wake, in which the strong temperature gradient concentrated around the vertical cores and was transported by the shed vortices downstream. The three tandem cylinders vibrated extensively in the streamwise and transverse directions. As a result, the wake interference regimes can change abruptly during the structural vibration intermittently. It was found that the transverse vibration amplitude of the upstream cylinder is close to that of an isolated vibrating cylinder with the same dimensionless groups. By contrast, the intensive structural vibration of the middle and downstream cylinders was excited at higher reduced velocity values; especially, their transverse vibrating amplitudes were found much higher than those upstream cylinders or an isolated cylinder. The Pearson correlation coefficient was used to determine the phase angle difference Φ between the lift force and the transverse vibration amplitude at the same frequency. The quantification of this phase angle difference directly reveals the status of kinetic energy transfer between fluid and the vibration structure, which is meaningful to the design of hydrodynamic energy harvester. The analysis of continuous wavelet transform results has shown that the change of heat convection (Nusselt number) over each cylinder surface is primarily dominated by the drag force for the low reduced velocity values, whereas it is significantly affected by the lift force for high reduced velocity values instead. Further extensive studies are required to investigate the thermal-induced vibration response of three tandem cylinders in detail in order to uncover the mechanism of complex coupling between fluid, elastic structure, and thermal convection in the flow regimes of much higher Reynolds numbers.

ACKNOWLEDGMENTS

This research was supported by the National Natural Science Foundation of China (Grant No. 51979238) and the Graduate Research Innovation Fund project of Southwest Petroleum University (Grant No. 2021CXYB52). The work was carried out in the computer cluster of the laboratory of offshore oil and gas engineering at Southwest Petroleum University.

AUTHOR DECLARATIONS

Conflict of Interest

The authors have no conflicts to disclose.

Author Contributions

Hongjun Zhu: Conceptualization (equal); Funding acquisition (equal); Supervision (equal); Writing – original draft (equal); Writing – review

and editing (equal). **Jiawen Zhong:** Conceptualization (equal); Data curation (equal); Formal analysis (equal); Investigation (equal); Validation (equal); Writing – original draft (equal). **Bin Liu:** Methodology (equal); Software (equal); Writing – review and editing (equal).

DATA AVAILABILITY

The data that support the findings of this study are available from the corresponding author upon reasonable request.

REFERENCES

[1]G. E. Karniadakis, "Numerical simulation of forced convection heat transfer from a cylinder in crossflow," Int. J. Heat Mass Transfer **31**, 107–118 (1988).
[2]R. D. Henderson, "Nonlinear dynamics and pattern formation in turbulent wake transition," J. Fluid Mech. **352**, 65–112 (1997).
[3]C. Norberg, "Flow around a circular cylinder: Aspects of fluctuating lift," J. Fluids Struct. **15**, 459–469 (2001).
[4]J. S. Wang, D. X. Fan, and K. Lin, "A review on flow-induced vibration of offshore circular cylinders," J. Hydrodyn. **32**, 415–440 (2020).
[5]X. Huang, H. Qi, F. Cai, Z. Feng, S. Liu, and Q. Huang, "Study on flow induced vibration analysis and evaluation for heat transfer tube of steam generator," in *Proceedings of the ASME 2018 Pressure Vessels and Piping Conference* (American Society of Mechanical Engineers, 2018), Vol. 51654, p. V004T04A009.
[6]E. Schmidt and K. Wenner, "Heat transfer over the circumference of a heated cylinder in transverse flow," Technical Report No. NACA-TM-1050, 1943.
[7]R. M. Fand, "Heat transfer by forced convection from a cylinder to water in crossflow," Int. J. Heat Mass Transfer **8**, 995–1010 (1965).
[8]K. Sreenivasan and A. Ramachandran, "Effect of vibration on heat transfer from a horizontal cylinder to a normal air stream," Int. J. Heat Mass Transfer **3**, 60–67 (1961).
[9]D. Karanth, G. W. Rankin, and K. Sridhar, "A finite difference calculation of forced convective heat transfer from an oscillating cylinder," Int. J. Heat Mass Transfer **37**, 1619–1630 (1994).
[10]C. H. Cheng, J. L. Hong, and W. Aung, "Numerical prediction of lock-on effect on convective heat transfer from a transversely oscillating circular cylinder," Int. J. Heat Mass Transfer **40**, 1825–1834 (1997).
[11]C. Gau, J. M. Wu, and C. Y. Liang, "Heat transfer enhancement and vortex flow structure over a heated cylinder oscillating in the crossflow direction," J. Heat Transfer **121**, 789–795 (1999).
[12]Z. Yang, L. Ding, L. Zhang, L. Yang, and H. He, "Two degrees of freedom flow-induced vibration and heat transfer of an isothermal cylinder," Int. J. Heat Mass Transfer **154**, 119766 (2020).
[13]B. Keshavarzian and M. Khosravi, "Numerical investigation of the structural frequencies effects on flow induced vibration and heat transfer," J. Mater. Environ. Sci. **6**, 1949–1956 (2015).
[14]S. K. Wang, T. C. Hung, G. W. Lin, and B. S. Pei, "Numerical simulations for the phenomena of vortex-induced vibration and heat transfer of a circular cylinder," Numer. Heat Transfer, Part A **45**, 719–736 (2004).
[15]F. Baratchi, M. Saghafian, and B. Baratchi, "Numerical investigation on lock-in condition and convective heat transfer from an elastically supported cylinder in a cross flow," J. Fluids Eng. **135**, 031103 (2013).
[16]E. Izadpanah, Y. Amini, and A. Ashouri, "A comprehensive investigation of vortex induced vibration effects on the heat transfer from a circular cylinder," Int. J. Therm. Sci. **125**, 405–418 (2018).
[17]T. Igarashi, "Characteristics of the flow around two circular cylinders arranged in tandem: 1st report," Bull. JSME **24**, 323–331 (1981).
[18]T. Igarashi, "Characteristics of the flow around two circular cylinders arranged in tandem: 2nd report—Unique phenomenon at small spacing," Bull. JSME **27**, 2380 (1984).
[19]M. M. Zdravkovich, "Review of flow interference between two circular cylinders in various arrangements," J. Fluids Eng. **99**, 618–633 (1977).
[20]M. M. Zdravkovich, "The effects of interference between circular cylinders in cross flow," J. Fluids Struct. **1**, 239–261 (1987).
[21]M. M. Zdravkovich, "Review of interference-induced oscillations in flow past two parallel circular cylinders in various arrangements," J. Wind Eng. Ind. Aerodyn. **28**, 183–199 (1988).
[22]M. M. Alam, M. Moriya, K. Takai, and H. Sakamoto, "Fluctuating fluid forces acting on two circular cylinders in a tandem arrangement at a subcritical Reynolds number," J. Wind Eng. Ind. Aerodyn. **91**, 139–154 (2003).
[23]H. Zhu and K. Wang, "Wake adjustment and vortex-induced vibration of a circular cylinder with a C-shaped plate at a low Reynolds number of 100," Phys. Fluids **31**, 103602 (2019).
[24]H. Zhu, J. Zhong, and T. Zhou, "Wake structure characteristics of three tandem circular cylinders at a low Reynolds number of 160," Phys. Fluids **33**, 044113 (2021).
[25]W. Chen, C. Ji, J. Williams, D. Xu, L. Yang, and Y. Cui, "Vortex-induced vibrations of three tandem cylinders in laminar cross-flow: Vibration response and galloping mechanism," J. Fluids Struct. **78**, 215—238 (2018).
[26]Y. Gao, Y. Zhang, M. Zhao, and L. Wang, "Numerical investigation on two degrees-of-freedom flow-induced vibration of three tandem cylinders," Ocean Eng. **201**, 107059 (2020).
[27]J. Tu, X. Tan, X. Deng, Z. Han, M. Zhang, Z. Li, J. Xu, and P. Zhang, "Dynamic responses and flow-induced vibration mechanism of three tandem circular cylinders in planar shear flow," Ocean Eng. **199**, 107022 (2020).
[28]N. Mahir and Z. Alta ç , "Numerical investigation of convective heat transfer in unsteady flow past two cylinders in tandem arrangements," Int. J. Heat Fluid Flow **29**, 1309–1318 (2008).
[29]R. C. Patil, R. P. Bharti, and R. P. Chhabra, "Forced convection heat transfer in power law liquids from a pair of cylinders in tandem arrangement," Ind. Eng. Chem. Res. **47**, 9141–9164 (2008).
[30]X. Sun, S. Li, G. G. Lin, and J. Z. Zhang, "Effects of flow-induced vibration on forced convection heat transfer from two tandem circular cylinders in laminar flow," Int. J. Mech. Sci. **195**, 106238 (2021).
[31]N. Mahir and Z. Alta ç , "Numerical investigation of flow and heat transfer characteristics of two tandem circular cylinders of different diameters," Heat Transfer Eng. **38**, 1367–1381 (2017).
[32]F. Zafar and M. M. Alam, "A low Reynolds number flow and heat transfer topology of a cylinder in a wake," Phys. Fluids **30**, 083603 (2018).
[33]I. Harimi and M. Saghafian, "Numerical simulation of fluid flow and forced convection heat transfer from tandem circular cylinders using overset grid method," J. Fluids Struct. **28**, 309–327 (2012).
[34]M. Shaaban and A. Mohany, "Flow-induced vibration of three unevenly spaced in-line cylinders in cross-flow," J. Fluids Struct. **76**, 367–383 (2018).
[35]B. Liu and H. Zhu, "Secondary lock-in of vortex-induced vibration and energy transfer characteristics of a vibrating cylinder subject to cross buoyancy," Phys. Fluids **33**, 073607 (2021).
[36]J. Chung and G. M. Hulbert, "A time integration algorithm for structural dynamics with improved numerical dissipation: The generalized-α method," J. Appl. Mech. **60**, 371–375 (1993).
[37]K. E. Jansen, C. H. Whiting, and G. M. Hulbert, "A generalized-α method for integrating the filtered Navier–Stokes equations with a stabilized finite element method," Comput. Methods Appl. Mech. Eng. **190**, 305–319 (2000).
[38]T. K. Prasanth, S. Behara, S. P. Singh, R. Kumar, and S. Mittal, "Effect of blockage on vortex-induced vibrations at low Reynolds numbers," J. Fluids Struct. **22**(6–7), 865–876 (2006).
[39]M. Zhao, F. Tong, and L. Cheng, "Numerical simulation of two-degrees-of-freedom vortex-induced vibration of a circular cylinder between two lateral plane walls in steady currents," J. Fluid Eng. **134**, 104501 (2012).
[40]G. Juncu, "A numerical study of momentum and forced convection heat transfer around two tandem circular cylinders at low Reynolds numbers. Part II. Forced convection heat transfer," Int. J. Heat Mass Transfer **50**, 3799–3808 (2007).
[41]S. Sarkar, A. Dalal, and G. Biswas, "Unsteady wake dynamics and heat transfer in forced and mixed convection past a circular cylinder in cross flow for high Prandtl numbers," Int. J. Heat Mass Transfer **54**, 3536–3551 (2011).
[42]S. W. Churchill and M. Bernstein, "A correlating equation for forced convection from gases and liquids to a circular cylinder in crossflow," J. Heat Transfer **99**, 300–306 (1977).

[43]J. Wu, C. Shu, and N. Zhao, "Numerical investigation of vortex-induced vibration of a circular cylinder with a hinged flat plate," Phys. Fluids **26**, 063601 (2014).
[44]Y. Bao, D. Zhou, and J. Tu, "Flow interference between a stationary cylinder and an elastically mounted cylinder arranged in proximity," J. Fluids Struct. **27**, 1425–1446 (2011).
[45]I. Borazjani and F. Sotiropoulos, "Vortex-induced vibrations of two cylinders in tandem arrangement in the proximity–wake interference region," J. Fluid Mech. **621**, 321–364 (2009).
[46]H. Zhu, G. Li, and J. Wang, "Flow-induced vibration of a circular cylinder with splitter plates placed upstream and downstream individually and simultaneously," Appl. Ocean. Res. **97**, 102084 (2020).
[47]R. Govardhan and C. H. K. Williamson, "Modes of vortex formation and frequency response of a freely vibrating cylinder," J. Fluid Mech. **420**, 85–130 (2000).
[48]F. Zafar and M. M. Alam, "Mixed convection heat transfer from a circular cylinder submerged in wake," Int. J. Mech. Sci. **183**, 105733 (2020).